Accepted Manuscript

Cassini-VIMS observations of Saturn's main rings: II. A spectrophotometric study by means of Monte Carlo ray-tracing and Hapke's theory.

M. Ciarniello, G. Filacchione, E. D'Aversa, F. Capaccioni,
P.D. Nicholson, J.N. Cuzzi, R.N. Clark, M.M. Hedman,
C.M. Dalle Ore, P. Cerroni, C. Plainaki, L.J. Spilker

Please cite this article as: M. Ciarniello, G. Filacchione, E. D'Aversa, F. Capaccioni, P.D. Nicholson, J.N. Cuzzi, R.N. Clark, M.M. Hedman, C.M. Dalle 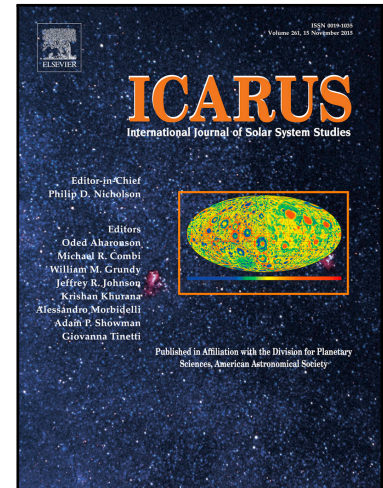Ore, P. Cerroni, C. Plainaki, L.J. Spilker, Cassini-VIMS observations of Saturn's main rings: II. A spectrophotometric study by means of Monte Carlo ray-tracing and Hapke's theory., *Icarus* (2018), doi: https://doi.org/10.1016/j.icarus.2018.07.010

Highlights

- Ring spectrophotometric behaviour is investigated on VIMS-Cassini radial mosaics.

- Light scattering models are used to infer ring composition and physical properties.

- A mixture of water ice, tholins and a broad-band absorber(s) provides the best-fit.

- The distribution of the broad-band absorber(s) is compatible with an exogenous origin.

- Tholins? distribution suggests an intrinsic origin.

1

Cassini-VIMS observations of Saturn's main rings: II. A spectrophotometric study by means of Monte Carlo ray-tracing and Hapke's theory.

M. Ciarniello[a], G. Filacchione[a], E. D'Aversa[a], F. Capaccioni[a], P. D. Nicholson[b], J. N. Cuzzi[c], R. N. Clark[d], M. M. Hedman[e], C. M. Dalle Ore[f], P. Cerroni[a], C. Plainaki[g], L. J. Spilker[h]

[a]IAPS-INAF, via Fosso del Cavaliere, 100, 00133, Rome, Italy
[b]Cornell University, Astronomy Department, 418 Space Sciences Building, Ithaca, NY 14853, USA
[c]NASA Ames Research Center, Moffett Field, CA 94035-1000, USA
[d]Planetary Science Institute, USA
[e]Physics Department, University of Idaho, Moscow, ID 83844, USA
[f]Carl Sagan Center, SETI institute, 189 Bernardo Ave, Suite 100, Mountain View, CA 94043
[g]Agenzia Spaziale Italiana, via del Politecnico, snc, 00133, Rome, Italy
[h]Jet Propulsion Laboratory, California Institute of Technology, Pasadena, CA 91109, USA

Abstract

This work is the second in a series of manuscripts devoted to the investigation of the spectrophotometric properties of Saturn's rings from Cassini-VIMS (Visible and Infrared Mapping Spectrometer) observations. The dataset used for this analysis is represented by ten radial spectrograms of the rings which have been derived in Filacchione et al. (2014) by radial mosaics produced by VIMS. Spectrograms report the measured radiance factor I/F of the main rings of Saturn as a function of both radial distance (from 73.500 to 141.375 km) and wavelength (0.35-5.1 μm) for different observation geometries (phase angle ranging in the $2° - 132°$ interval). We take advantage of a Monte Carlo ray-tracing routine (Ciarniello et al., 2014) to characterize the photometric behavior of the rings at each wavelength and derive the spectral Bond albedo of ring particles. This quantity is used to infer the composition of the regolith covering ring particles by applying Hapke's theory. Four different regions, characterized by different optical depths, and respectively located in the C ring, inner B ring, mid B ring and A ring, have been investigated. Results

from photometric modeling indicate that, in the VIS-NIR spectral range, B ring particles are intrinsically brighter than A and C ring particles, with the latter having the lowest albedo, while the single particle phase function of the ring's particles is compatible with an Europa-like or Callisto-like formulation, depending on the investigated region. Spectral modeling of the inferred Bond albedo indicates that ring spectrum can be reproduced by water ice grains with inclusion of organic materials (tholin) as a UV absorber intimately mixed with variable amounts of other compounds in pure form (carbon, silicates) or embedded in water ice grains (nanophase hydrated iron oxides, carbon, silicates, crystalline hematite, metallic iron, troilite). The abundance of tholin decreases with radial distance from C ring (0.2-0.6%) to A ring (0.06%) for the selected regions. Its distribution is compatible with an intrinsic origin and is possibly related to the different plasma environment of the different ring regions. The identification of the other absorber(s) and its absolute volumetric abundance is uncertain, depending on the adopted grain size and mixing modality (intraparticle or intimate). However, assuming a common composition of the other absorber in the ring plane, we find that its abundance anti-correlates with the optical depth of the investigated regions, being maximum in the thinnest C ring and minimum in the thickest mid B ring. In the case of the C ring, an additional population of low-albedo grains is required to match the positive spectral slope of the continuum in the 0.55-2.2 μm interval, represented by an intraparticle mixture of water ice and a spectrum similar to troilite or metallic iron. The distribution of the darkening compounds is interpreted as the result of a contamination by exogenous material, which is more effective in the less dense regions of the rings because of their lower surface mass density of pure water ice.

Keywords: Saturn, rings, Radiative transfer, Spectrophotometry

---

1. Introduction

The Cassini spacecraft has been orbiting in the the Saturnian system since 2004. After the period of the nominal mission (July 2004 - June 2008), the activity of the spacecraft was extended up to 2010 (Cassini-Huygens Equinox Mission) and has completed the third and final stage (Cassini Solstice) by September 15, 2017. During this long period the VIMS (Visible Infrared Mapping Spectrometer) instrument acquired a large spectral dataset of the Saturnian rings. The VIMS experiment (Brown et al., 2004; McCord et al.,

2004) consists of two imaging spectrometers: VIMS-V and VIMS-IR. The first one covers the VIS-NIR range (0.35-1.05 μm) using 96 spectral channels with a sampling of ≈ 7.3 $nm/band$ and instantaneous field of view (IFOV) of 500 $\mu rad \times$ 500 μrad (nominal) or 166 $\mu rad \times$ 166 μrad (high resolution). The latter works at infrared wavelengths (0.885-5.1 μm, 256 channels, Miller et al. (1996)) with 16 $nm/band$ spectral sampling and IFOV of 500 $\mu rad \times$ 500 μrad (nominal) or 250 $\mu rad \times$ 500 μrad (high resolution). The spectral capabilities of the instrument allowed the investigation of the composition of the different regions of the rings characterizing the physical properties of the regolith which covers the ring particles as shown in Nicholson et al. (2008); Cuzzi et al. (2009); Filacchione et al. (2012); Hedman et al. (2013). The results of these studies indicate that Saturn's rings are composed mainly of water ice with grain size from tenths to hundreds of microns (Nicholson et al., 2008; Filacchione et al., 2012) contaminated by the presence of a darker component absorbing the light in the UV region, whose origin (organic or mineral) is still debated (Poulet et al., 2002a; Poulet and Cuzzi, 2002; Clark et al., 2012). Along with these spectral studies many works investigated the photometry of the rings at visible wavelengths and small phase angles mainly using observations from Hubble Space Telescope (Cuzzi et al., 2002; Poulet et al., 2002b; French et al., 2007a,b; Déau et al., 2009; Salo and French, 2010) and from Cassini (Déau et al., 2013; Déau, 2015). The study of the rings phase curve at large phase angle has been described in Dones et al. (1993) and Salo and Karjalainen (2003) using Voyager data and by Déau (2015) using Cassini images.

The photometric behavior of the rings is typically described assuming that single scattering is the dominant process in the light-particle interaction (Dones et al., 1993; Cuzzi et al., 2002), using what we define here as a "classical" approach, and neglecting the contribution from inter-particle radiative scattering. These models, as described in Sec. 2 have the advantage of being analytical and provide a relatively good approximation of ring photometry at Earth-based observation geometries when particle albedo is moderate and the filling factor of the ring plane ϕ (i.e. the fraction of volume occupied by particles) is small. Conversely, at large phase angles, the classical equation which describes ring reflectivity (I/F) is applicable only for low optical depth (τ) regions (with $I/F \propto \tau$) where multiple scattering, typically significant in the forward scattering regime, can be considered as negligible (Cuzzi et al., 2002).

An alternative approach, able to overcome the limitations imposed by the

4

single scattering approximation, is given by Monte Carlo ray-tracing. This method, as shown in Salo and Karjalainen (2003); Salo et al. (2004); Stankevich and Shkuratov (2004); Shkuratov et al. (2005); Salo and French (2010) represents a powerful tool to describe light scattering in particulate media in the geometric optics limits. The advantage of numerical simulations with respect to the classical analytical methods is that the physical properties of the medium (filling factor, optical depth, particle size distribution, particle albedo and particle phase function) can be accurately described, and their effects on the final output can be studied in more detail. Moreover, a Monte Carlo approach gives the possibility to explore variable observations geometries, from small to large phase angles. Of course the limitation of this technique is represented by the computational time, that in the most complex cases can be fairly long.

In this work, we use the Monte Carlo ray-tracing method described in Ciarniello et al. (2014) to investigate the photometric behavior of Saturn's rings as seen by VIMS, in order to infer their physical properties and study the dependence of ring spectra on observation geometry, comparing the simulations to real data. This approach allows us to determine the spectral Bond albedo of ring particles in the instrument wavelength range and this quantity will be used to derive the composition of the regolith covering the surface of ring particles by applying Hapke's model (Hapke, 1993; Ciarniello et al., 2011).

In Sec. 2 the "classical" single scattering analytical model will be discussed and compared to the results of the Monte Carlo simulations. The VIMS dataset analyzed in this work is described in Sec. 3 and the methods adopted to determine the ring Bond albedo spectrum and derive regolith composition are in Sec. 4. Results from the comparison between observations and computer simulations are reported in Sec. 5 while a discussion of the dependence of the spectral behavior on the phase angle is in Sec. 6. In Sec. 7 the outcome of the spectral fitting and the derived ring composition are discussed. Finally, we summarize the results of this study in Sec. 8.

2. Limits of the single scattering approximation

The radiative transfer equation for a finite particulate medium like the ring plane can be solved analytically in the case of single scattering approximation (Chandrasekhar, 1960). Under this assumption, the radiance factor

5

$\frac{I}{F}$ of the lit side of the rings can be expressed by the following equation:

$$\frac{I}{F}(i, e, g, \lambda) = \frac{A_S(\lambda)}{4\pi} \frac{\mu_0}{\mu_0 + \mu} P(g, \lambda)(1 - e^{-\tau \frac{\mu_0 + \mu}{\mu_0 \mu}}) \quad (1)$$

$$\mu_0 = \cos(i)$$

$$\mu = \cos(e)$$

where i, e and g are the incidence, emission and solar phase angles with respect to the plane of the rings, A_s the spectral Bond albedo (e.g total fraction of incident irradiance at a given wavelength λ scattered by a body into all directions (Hapke, 1993)), $P(g)$ the single particle phase function (SPPF), and τ the optical depth. In this section we investigate under which conditions, in terms of observation geometry, optical depth and filling factor, this equation can be rigorously applied. In order to perform this task we make use of a Monte Carlo ray-tracing routine as described in Ciarniello et al. (2014). In this approach the path of each single photon packet is traced from the Sun to the observer after interaction with ring particles. The output of the routine is the reflectance of the rings in a given geometry, which is proportional to the total energy carried by the photon packets reaching the observer. The ring is modeled as a slab of spherical particles with given A_s and SPPF. In the routine, the A_s represents the fraction of energy of the photon packet surviving at each scattering, while the SPPF determines statistically the direction of the scattered photons. The depth of the slab is adjusted to match the optical depth for a certain filling factor. For given configurations of observation geometry and ring structure, we compare Monte Carlo simulations with results from eq. 1. In all the simulations we assume solar elevation angle $\beta = 20°$ ($i = 70°$) because this value is typical for the Saturn's rings illumination conditions of the dataset used in this work (see Sec. 3). We model the ring plane assuming combinations of optical depth and filling factors in the following ranges:

- $\phi = [0.01, 0.1]$

- $\tau = [0.1, 2]$

and adopting a Callisto-like single particle phase function (see Sec. 4). This formulation of the SPPF has been shown to approximate the ring photometric properties (Dones et al., 1993). Results are summarized in Fig. 1. The

6

simulated phase curves are positively correlated with the Bond albedo and show the expected global behavior of the I/F as a decreasing function of the phase angle. The surge of the signal at small phase angles commonly referred to as opposition effect (OE) can also be recognized. This phenomenon primarily depends on inter-particle shadowing and, as shown in the simulations, it is more significant when optical depth approaches unity (producing a more intense surge) and filling factors are relatively large (affecting a larger interval of phase angles around $0°$). It is worth mentioning that the OE can also be produced by intrinsic effects taking place in the regolith covering the ring particles, like shadow hiding and coherent backscattering, as reported in Salo and French (2010).

From the comparison between Monte Carlo simulations and the predicted output of eq. 1 it can be noted that the single scattering approximation holds for low Bond albedos, with the exception of the opposition effect (OE) region which needs to be modeled independently (French et al., 2007b; Salo and French, 2010) and the portion of the phase curve at very large absolute values of the emission angle, where an increase of the output can be observed in the simulations. For increasing A_s the match worsens because of the growing contribution of multiple scattering which dominates at large phase angles (Dones et al., 1993; Salo and Karjalainen, 2003) and increases with τ. This indicates that for observations acquired at low-intermediate phase angles eq. 1 satisfactory describes the photometry of the rings in the low-albedo regime, but this is not the case of Cassini data, which span across a large set of phase angles and observation geometries ($\approx 1° - 130°$), thus requiring the adoption of a different approach, which in this work is represented by Monte Carlo ray-tracing. Concerning the effect of the filling factor, the simulations point out that it mostly affects the OE region. Along with this, an increase of the overall albedo with ϕ can also be noted, in particular for the smallest optical depths. We attribute this to the fact that, for a given optical depth, larger values of ϕ correspond to a ring structure progressively more similar to a monolayer, with the most of the signal produced by light scattered by the upper portion of the particles. In this configuration, light scattered by one particle has a lower probability of being intercepted by others with respect to the case of a low-filling factor and vertically-extend ring. This also explains the difference between simulations and the output produced by eq. 1, in particular for the low optical depths. In fact, although at these values of τ the output is driven by single scattering, eq. 1 is derived to model light scattering in a many-particle thick medium.
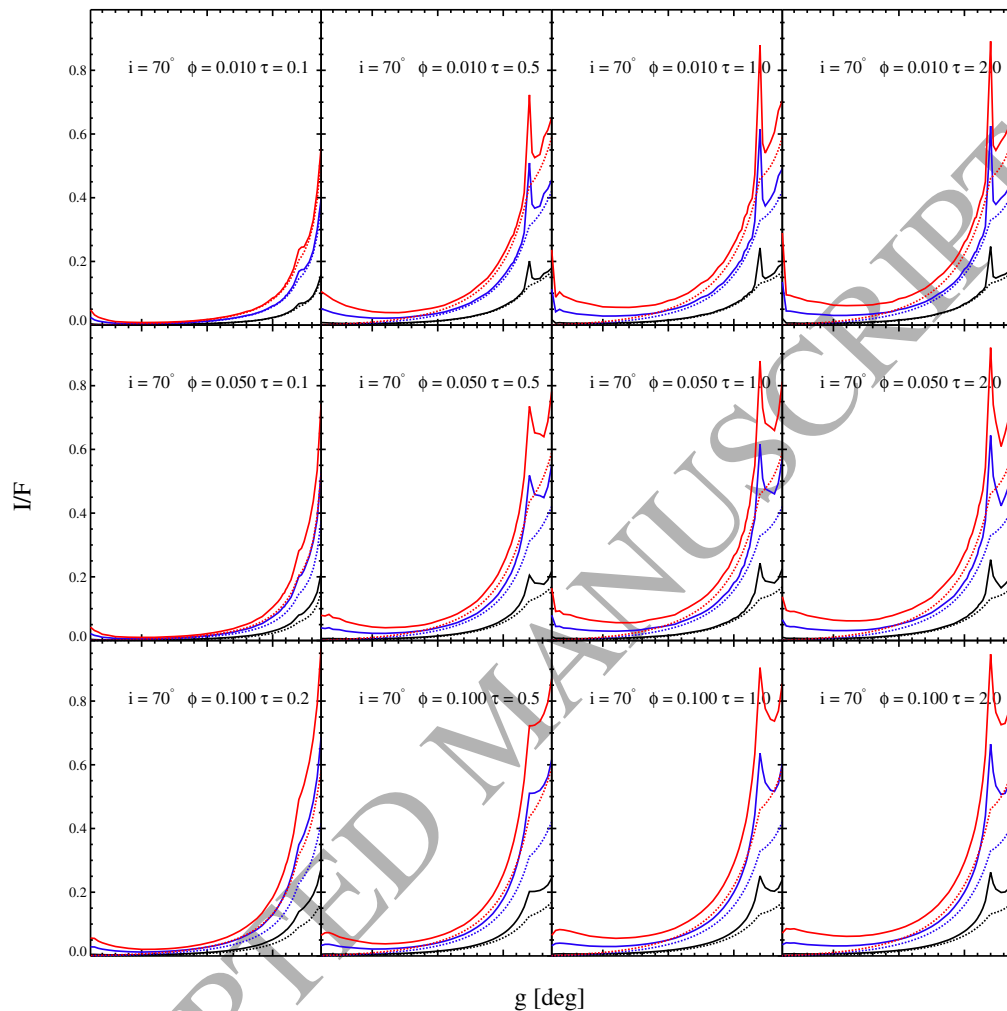
7

Figure 1: Simulated reflectance curves as a function of emission angle. A Callisto-like SPPF is assumed. Incidence angle is $i = 70°$ for all simulations, filling factor ϕ increases from top to bottom and optical depth τ from left to right. Notice that τ is set to 0.2 in the bottom-left panel, instead of 0.1 as for the other plots in the same column: this is due to the fact that for a monodisperse distribution of spherical particles with $\phi = 0.1$ the minimum achievable τ is ≈ 0.16. The scattering plane contains the normal at the surface of the rings and both the incidence and emission directions are relative to the lit side of the ring plane. Emission angle is reported as negative for light emitted on the opposite side of the illumination direction, with respect to the normal. The phase angle is then $g = |i - e|$. Data from Monte Carlo simulations are shown with solid lines while dotted lines refer to eq. 1. In each plot, three set of curves are drawn for $A_S = 0.2, 0.5, 0.7$, in black, blue and red, respectively.

8

3. Ring spectrograms

In Filacchione et al. (2014), VIMS data[1] of the Saturnian rings from 10 observation sequences have been rearranged to compose radial mosaics at different observations geometries with a radial binning of 400 km, spanning from 73500 km (D ring external edge) up to 141375 km (F ring) of Saturn radial distance. The collection of these mosaics at each wavelength of the VIMS range (0.35-5.1 μm) for a single observation sequence is referred to as spectrogram. Each spectrogram is a matrix with two dimensions: radial and spectral. It allows investigating the spectral properties of the rings as a function of the distance from Saturn. As stated above, spectrograms have been produced for different observation sequences that correspond to different observation geometries (Sun illumination angle, emission angle and phase angle) as well as spatial resolutions at the ring plane. For a given wavelength and radial position R it is then possible to retrieve an $I/F(\lambda)$ profile as a function of the observation geometry (e.g. phase angle) as shown in Fig. 2. The error associated to the reflectance for each spectrogram was derived in Filacchione et al. (2014) accounting for the raw average signal measured in each radial bin and the average sky level, and it is below 1% in the range 0.35-2.5 μm where signal is larger, increasing up to $15-20\%$ at longer wavelengths, where the typical spectrum of the rings has lower radiance values. The level of noise increases for spectrograms acquired at large phase angles because of reduction of the photometric output at these geometries. Along with this, other sources of uncertainty on the derived reflectance can be considered:

- spectrograms are computed by means of azimuthal averages taken on the proximity of the ring ansa, thus azimuthal asymmetries (French et al., 2007a; Salo et al., 2004) can increase the dispersion;

- depending on the spacecraft-rings distance, the pixel projection on the ring plane can be larger than the radial binning, in particular at large emission angles, reducing the effective spatial resolution of the spectrogram and mixing the signal coming from different regions;

For these reasons the error reported in Filacchione et al. (2014) can be considered as a lower limit of the real uncertainties associated with the reflectance

---

[1]VIMS data used in Filacchione et al. (2014) have been calibrated by means of the RC17 version of the calibration pipeline (Clark et al., 2012), currently used at the time of the publication.
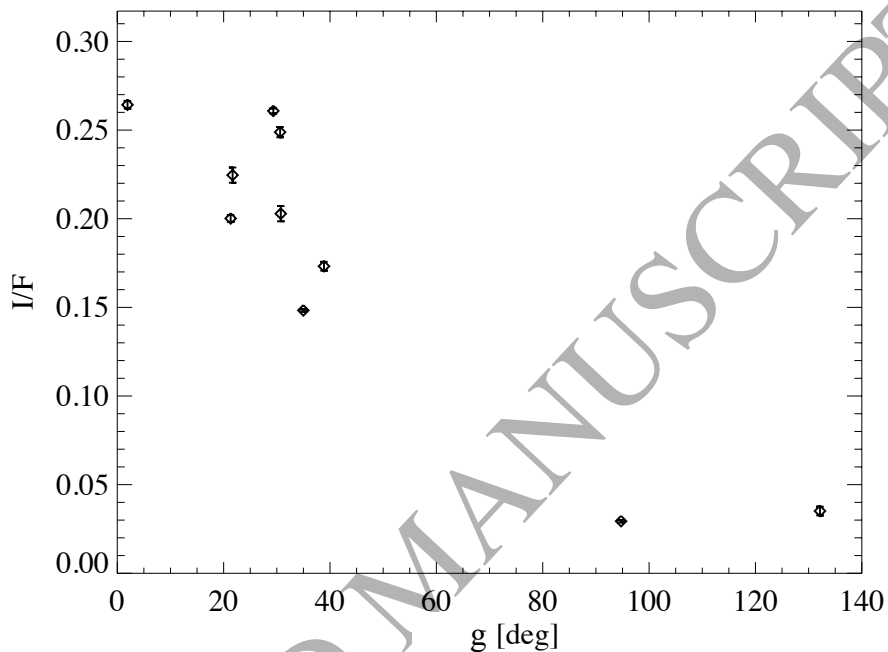
9

level in the spectrograms.

Figure 2: I/F scatterplot at 0.55 μm as a function of phase angle g for a region of the B ring at $R = 94300$ km. The points correspond to the ten VIMS observations analyzed in this work. The dispersion is caused by the different values of g, i and e characterizing each observations. Error bars are computed according to Filacchione et al. (2014).

4. From reflectance profiles to ring composition

Reflectance profiles derived from spectrograms give us the possibility to characterize the photometric properties of the rings (particle spectral Bond albedo and phase function) and to obtain clues on ring structure. This can be done by matching the observed reflectance with simulations produced by means of the Monte Carlo ray tracing code. The output of the simulations depends on the modeled ring optical depth, filling factor, SPPF and A_s. We assume as the optical depth for a given radial distance the one derived

10

from UVIS occultations (Fig. 3, Colwell et al. (2010)), while from the match between the measured profiles and the simulation we retrieve ϕ, SPPF and A_s.
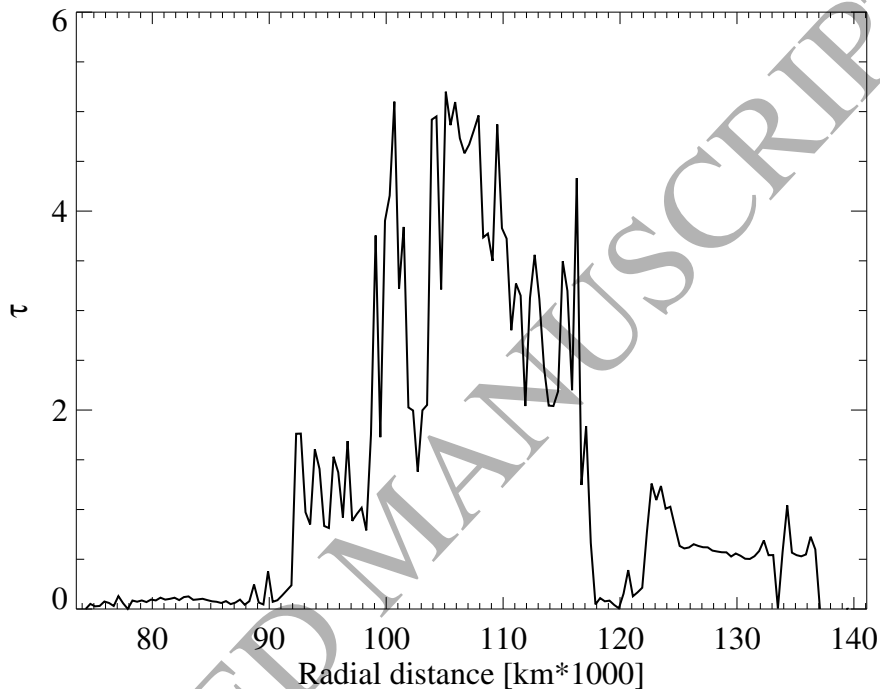

Figure 3: Optical depth profile of the rings from UVIS stellar occultations (Colwell et al., 2010) interpolated at VIMS rings' spectrograms 400 km radial scale.

Given the relatively long computational time of Monte Carlo simulations it was possible to explore only a limited number of the combinations of these quantities, then, for a given optical depth, we generated ring models combining selected filling factors (e.g. ring physical thickness) in the range 0.01-0.25 with three different SPPFs characterized by a progressive increment of back-scattering response: Lambertian, Europa-like and Callisto-like (Fig. 4). Such SPPFs have been already adopted in ring studies (Dones et al., 1993; Salo and French, 2010), given their behavior which is in better agreement with ring photometric properties with respect to more isotropic or forward scattering formulations.
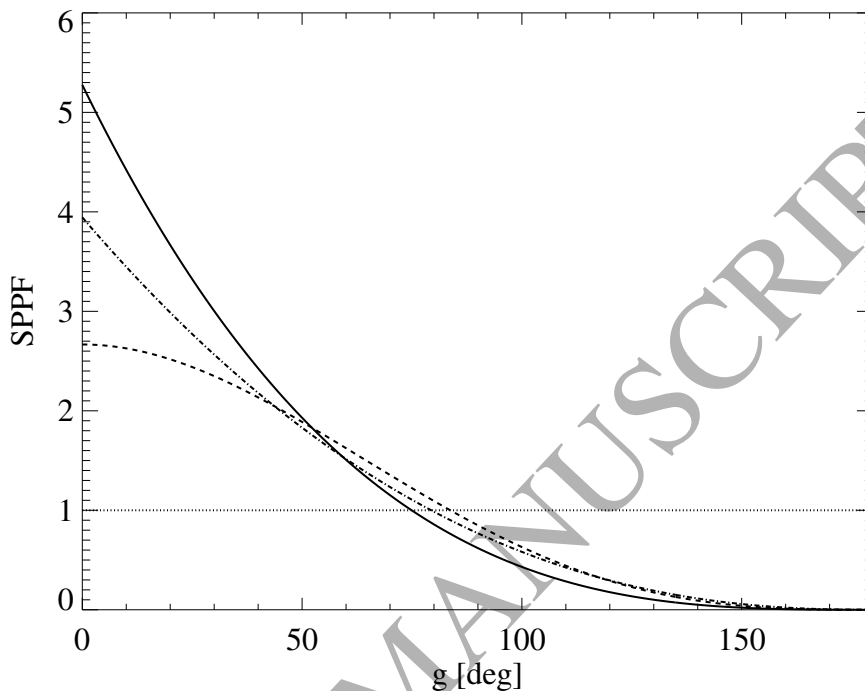
11

Figure 4: Single particle phase functions: Callisto-like (solid), Europa-like (dash-dotted) and Lambertian (dashed).The isotropic SPPF is reported for comparison (dotted).

For each model a simulation is produced, assuming the geometries of VIMS observations, for all the possible values of ring particle spectral Bond albedo in the 0-0.8 range (at step of 0.01). The result is a family of reflectance profiles which are compared to the measured one, wavelength by wavelength; a least square method applied to the phase curves for each wavelength was used to derive the best fit to the reflectance, thus determining the spectral Bond albedo, the single particle phase function and the filling factor of the investigated region. The result of this procedure allows us to decouple the photometric properties from the spectral ones that are described by the Bond albedo spectrum. To retrieve the compositional properties of the regolith which covers ring particle we finally model the spectral Bond albedo. The Bond albedo is the total fraction of incident irradiance scattered by a body in all directions. This definition can be applied also to ring particles; thus,

12

if the reflectance of each surface element of the particle is $r(i_p, e_p, g_p)$, the Bond albedo A_s is given by:

$$A_S = \frac{1}{\pi} \int_{2\pi} \int_{2\pi} r(i_p, e_p, g_p) \mu_p d\Omega_{i_p} d\Omega_{e_p} \qquad (2)$$

where i_p, e_p, g_p are the incidence, emission and phase angles of a given particle's surface element and $d\Omega_{i_p}$ and $d\Omega_{e_p}$ are the increments of solid angle along the incidence and emission directions, respectively. From an estimate of A_s is then possible to determine the physical properties of the surface if a model for $r(i_p, e_p, g_p)$ is provided. In this paper we achieve this task by using the Hapke model, whose formulation is reported below:

$$r(i_p, e_p, g_p) = \frac{w}{4\pi} \frac{\mu_{0p}}{\mu_{0p} + \mu_p} \left[p(g_p) + H(\mu_p, w)H(\mu_{0p}, w) - 1 \right] \qquad (3)$$

with $\mu_p = cos(e_p)$, $\mu_{0p} = cos(i_p)$ and where w is the single scattering albedo (SSA), $p(g_p)$ is the single grain phase function and $H(x, w)$ are the Chandrasekhar functions, which are involved in the computation of the multiple scattering contribution. In eq. 3 we omitted the opposition effect, surface roughness and porosity terms (Hapke, 2008, 2012; Ciarniello et al., 2014). The former can be ignored since its contribution to the integral in eq. 2 can be neglected, while the other two have been set to 1 in order to minimize the number of free parameters of the model.

It can be shown (Van de Hulst, 1974) that in the case of an isotropic scattering surface, $p(g_p) = 1$, the Bond albedo can be expressed as:

$$A_S = 1 - \gamma H_1 \qquad (4)$$

where $\gamma = \sqrt{1-w}$ and $H_1 = \int_0^1 xH(x)dx$ is the first momentum of the Chandrasekhar function. This expression can be extended to an anisotropic scattering surface by means of the similarity relations (Hapke, 1993), thus substituting w and γ by

$$w^* = \frac{1-b}{1-bw}w \qquad (5)$$

$$\gamma^* = \sqrt{1-w^*} \qquad (6)$$

where b is the asymmetry parameter of the single particle phase function, modeled with the Henyey-Greenstein equation (Henyey and Greenstein, 1941).

13

If the A_S of ring particles is known, it is possible to invert eq. 4 to retrieve the SSA (w). Recently, Cuzzi et al. (2018) propose an additional correction to the Bond albedo, before it is converted to SSA, with the aim to take into account for ring particles roughness. In our approach we do not include this effect, and this is discussed in Sec. 7.7. The SSA is directly linked to the composition of the investigated medium and can be modeled by means of Hapke's theory (Hapke, 2012) to determine the composition of the regolith covering ring particles (Ciarniello et al., 2011). This can be done straightfor-wardly by applying eq. 4 and 6 if a determination of b is given. In order to derive the asymmetry parameter, we consider a single ring particle, assumed as spherical. It scatters light following the relation below (Hapke, 2012):

$$I(\Omega) = J(\Omega_0)A_S\frac{P(g)}{4\pi} \tag{7}$$

where $I(\Omega)$ is the radiance scattered into Ω direction, $J(\Omega_0)$ is the solar irradiance coming from Ω_0 and $P(g)$ is the SPPF of the ring particle. We recall here that g is the observation phase angle of the ring plane and that necessarily $g = g_p$. The same quantity of eq. 7 can be expressed as follows

$$I(\Omega) = \frac{1}{\pi R_p^2} \int_{A(ill,vis)} J(\Omega_0)r(i_p,e_p,g_p)\mu_p dA \tag{8}$$

where $r(i_p, e_p, g_p)$ is the reflectance of the regolith, dA is a surface element, R_p the particle radius and $A(ill, vis)$ represents the portion of surface both illuminated and visible. Because $dA = R_p^2 d\Omega_p$ with $d\Omega_p$ the solid angle subtending dA, from the comparison between eq. 7 and 8 we can express the single particle phase function as:

$$P(g_p) = \frac{4}{A_S} \int_{A(ill,vis)} r(i_p,e_p,g_p)\mu_p d\Omega_p \tag{9}$$

The asymmetry parameter can then be determined as the value that inserted into $p(g_p)$ (modeled as the Heyney-Greenstein function) in the def-inition of $r(i_p, e_p, g_p)$ (eq. 3) provides the best match with eq. 9. Its value depends on the SSA (linked to A_s by eq. 6) and can be determined in a numerical way.

5. Photometric analysis

In this work we focus our analysis on four regions of the rings: the first pertains to C ring at $R = 81100$ km (C81100, $\tau = 0.094$), the second is

14

relative to a low density region in the B ring (R = 94300 km, B94300, τ = 1.4), the third is in the outer B ring, where the optical depth is larger (R = 106700, B106700, τ = 4.6) and the latter is in the A ring (R = 131900, A131900, τ = 0.6). Here we present the results of the comparison between measured reflectance profiles and simulated ones for all the positions defined above. As stated in Sec. 4 this method allows us to characterize the filling factor of the ring plane, the single particle phase function and eventually the spectral Bond albedo of the ring particles. In Fig. 5, as an example, different simulated reflectance profiles are shown for various filling factors and different single particle phase function, assuming the observation geometry and optical depth (τ = 1.4) of the $B94300$ region and A_S = 0.5. It can be noted that variations in the filling factors affect the shape of the reflectance profile and the overall output level as well, with an increase for larger ϕ, while the single particle phase function drives the global behavior with phase angle.

The comparison between measured reflectance profiles and simulations has been performed for all the wavelengths in the VIMS range. For each given combination of filling factor (i) and SPPF (j) we compute a cost function $C_{i,j}(\lambda)$ depending on the wavelength λ ,as follows:

$$C_{i,j}(\lambda) = \frac{\sum_g (I/F(\lambda, g) - I/F^{sim}_{i,j}(g, A_S(\lambda)_{i,j}))^2}{I/F^2(\lambda, g*)N_{obs}} \tag{10}$$

where g is the phase angle of each observation, I/F and $I/F^{sim}_{i,j}$ are the measured and simulated radiance factors respectively, $A_S(\lambda)_{i,j}$ is the best fit spectral Bond albedo for that combination of filling factor and phase function, $g*$ is the phase angle for a selected observation geometry and N_{obs} = 10 is the number of points in the phase curve. The quality of the resulting fit for a given combination of filling factor, SPPF and spectral Bond albedo $A_S(\lambda)_{i,j}$ is defined by the median residual over λ, Res = Median $[C_{i,j}(\lambda)]$. This quantity is considered in the evaluation of the accuracy of the different ring models, along with qualitative considerations concerning the global description of the measured photometric behavior. We notice here that, in principle, the ring particle phase function is a wavelength dependent quantity. However, our method selects an average behavior of the SPPF over the VIMS spectral range. In order to account for the wavelength dependence of SPPF we should be able to produce Monte Carlo models with a large number of different single particle phase function, which is impractical. Given this, our result must be considered as representative of the average spectrophotometric response of the investigated region.
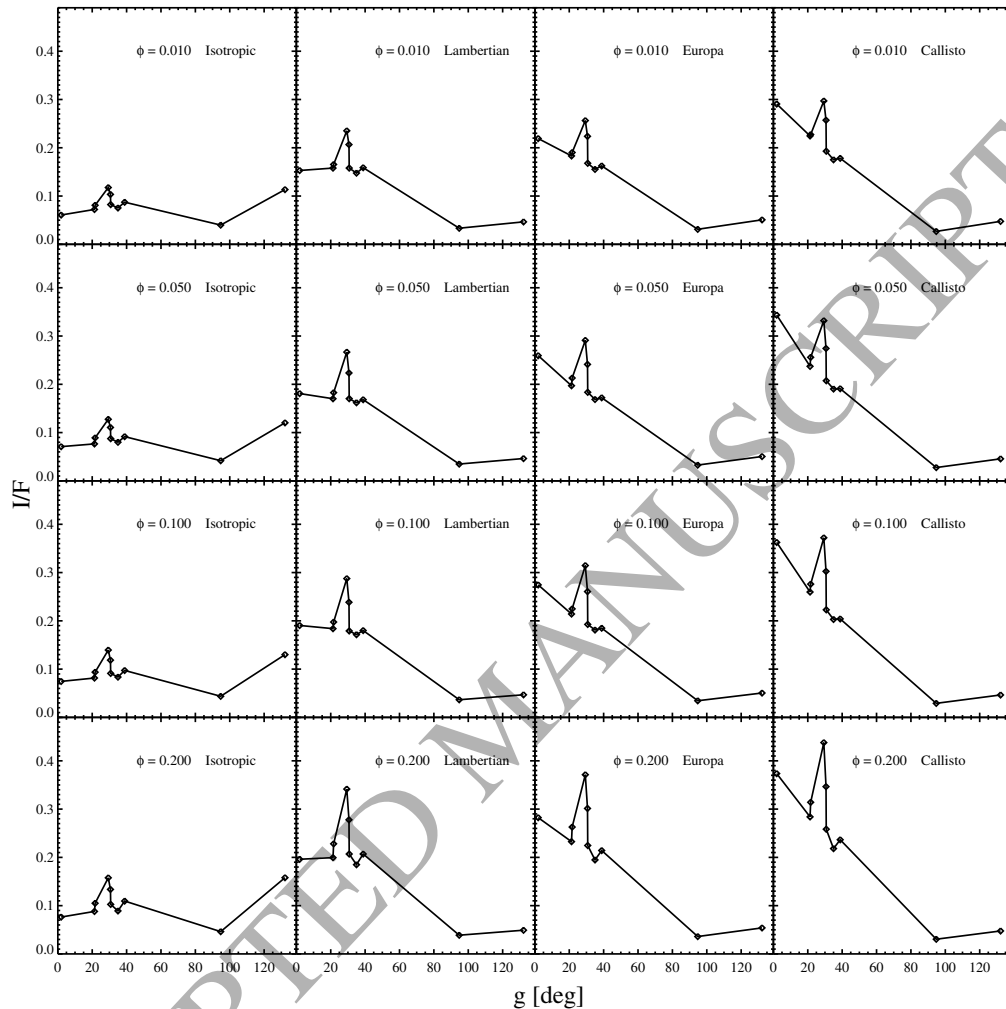
Figure 5: Simulated I/F as a function of the phase angle for various filling factors and phase functions (indicated in the plots) for the ten VIMS observations geometries relative to B94300 region with optical depth $\tau = 1.4$ and Bond albedo fixed to A_s=0.5. The dispersion of the points in each plot is caused by the different values of g, i and e characterizing the observations.

5.1. C81100

In Fig. 6, we report the best fits at $\lambda = 0.55\ \mu m$ for a series of investigated models for the selected region in the C ring. Given the low optical depth we explored a maximum filling factor of ≈ 0.04, which corresponds to a

16

ring depth of ≈ 1.5 times the particle size. Because of the marked back-scattering behavior of the measured reflectance curve only the Callisto and Europa SPPFs have been investigated. Although a best-fit model can be defined in terms of the *Res* parameter, it can be noted that more than one model provide a reasonably good match to the measured reflectance curve. This is due to the interplay among the ring filling factor, phase function and albedo. In particular a reduction of the filling factor is compensated by an increase of A_s and/or a more back-scattering SPPFs. The corresponding best-fit spectral A_s for each model is shown in Fig. 7. With the aim to provide a conservative estimate of the spectral Bond albedo we then define two possible solutions for A_s, which represent an upper and a lower limit of our derivation, by averaging separately the two solutions with the Callisto-like SPPF (C81100a), and the two with the Europa-like (C81100b) (Fig. 17).

5.2. B94300

In Fig. 8 and 9, we report the best fits at $\lambda = 0.55~\mu m$ for a series of investigated models for the selected region in the B ring. As for the C ring, given the backscattering behavior of the phase curve we explore only models with Callisto-like and Europa-like SPPF, while ϕ varies from 0.01 to 0.2. At first, similarly to Sec. 5.1, all the models have been produced assuming a constant filling factor vertical profile (indicated as *const* in the plots) in the ring plane (Fig. 8). However, Salo and Karjalainen (2003) and Salo and French (2010) suggest that in the B ring the filling factor may decrease as a function of the height z above the ring plane, due to a concentration of larger particles in the central layers. This should explain the "tilt-effect", which is the brighting of the rings at increasing emission angles (Lumme et al., 1983; Salo and French, 2010). A realistic vertical distribution of the particles in the rings can be obtained by means of N-body simulations (Salo, 1995; Salo et al., 2001) and is beyond the scope of this work, but we empirically accounted for this effect assuming a gaussian (indicated as *gauss* in the plots) distribution of the filling factor with z, in a second set of simulations (Fig. 9). In this case a maximum average filling factor $\phi = 0.15$ has been modeled, corresponding to a ring thickness of ≈ 5 particle diameters, which allows only a gross approximation of a gaussian profile. Larger average filling factors require smaller slab thickness, for which makes even less sense to define a gaussian filling factor profile.
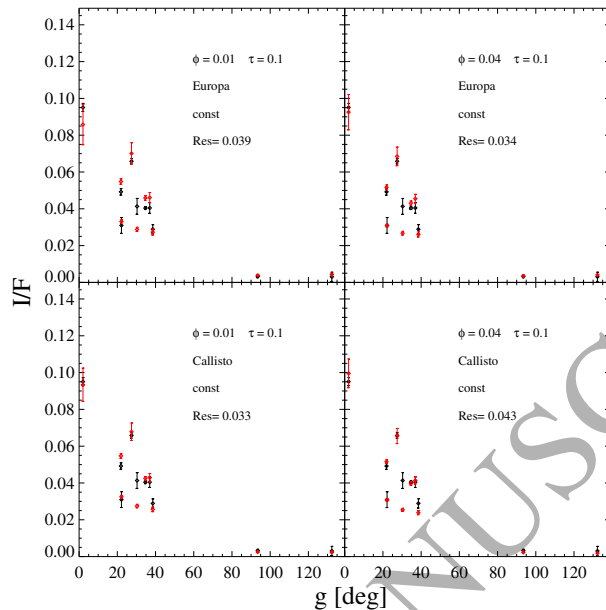
17

Figure 6: Fitted reflectance profiles at $\lambda = 0.55~\mu m$ for C81100 region (red: Monte Carlo models; black: VIMS data), for various filling factors and SPPFs, as indicated in the plots. The *const* label indicates that the filling factor profile is assumed as constant along the vertical direction in the ring plane (in Sec. 5.2 the use of a gaussian filling factor profile is also introduced). Error bars on Monte Carlo models are upper limits from uncertainties on observation geometry. The *Res* value is indicated and is calculated across the whole spectral range (see sec. 5).

The comparison between Fig. 8 e Fig. 9 indicates a global reduction of the *Res* value for the models described by a gaussian filling factor indicating the Callisto-like SPPF as the best fit, with different values of the average ϕ. However, two models based on the Europa-like SPPF (assuming constant and gaussian ϕ) provide comparable good fits. The corresponding spectral bond albedo of these models are shown in Fig. 10. As done for the C ring region we have averaged separately the best ($Res \leq 0.005$) Callisto-like (B94300a) models and Europa-like models (B94300b) and plotted them in Fig. 17. It can be noted that for increasing filling factors the retrieved A_s is typically smaller. It is important to mention that larger concentrations of particles in the ring mid-plane can be obtained by means of different vertical filling factor profiles and not uniform particle size distribution, and may potentially provide smaller best-fit A_s's. The exploration of further scenarios,
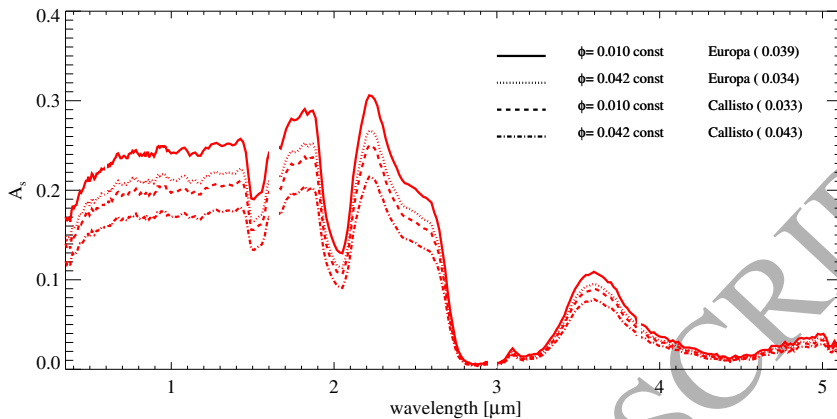
18

Figure 7: Best-fit spectral A_s's as derived from photometric fits of C81100 reflectance curves. The filling factor, phase function and *Res* value (in parenthesis) of the corresponding photometric models are indicated. The *const* label indicates that the filling factor profile is assumed as constant along the vertical direction in the ring plane (in Sec. 5.2 the use of a gaussian filling factor profile is also introduced). Missing parts of the spectrum correspond to the instrument order sorting filters junctions.

although meaningful for the aim of this study, is limited by computational time constraints.

5.3. B106700

In Fig. 11 and 12 we report the best fits at $\lambda = 0.55~\mu m$ for a series of investigated models for the optically thickest of the two selected regions in the B ring. With respect to the reflectance curve of the other studied regions, B106700 shows a less backscattering behavior. Given this, along with Callisto-like and Europa-like SPPFs, also models with a Lambertian phase function are considered. As for the B94300 region, we include models with both constant (Fig. 11) and gaussian (Fig. 12) filling factor profiles.

For all the investigated models the gaussian filling factor profile provides a better match to the observations, and among these we can select four solutions with comparable *Res* values ≤ 0.007. The corresponding spectral bond albedo is indicated in Fig. 13. These all pertain to models adopting Europa-like phase curves, and variable filling factors. In particular, it can be noted that solutions with the lowest ϕ (0.05-0.1) provide a better match at small phase angles, but are notably worse at high g where the I/F is largely

19

Figure 8: Fitted reflectance profiles at $\lambda = 0.55$ μm for B94300 region (red: Monte Carlo models; black: VIMS data), for various filling factors and SPPFs, as indicated in the plots. Filling factor profiles are assumed constant. Error bars on Monte Carlo models are upper limits from uncertainties on observation geometry. The *Res* value is indicated and is calculated across the whole spectral range (see sec. 5).
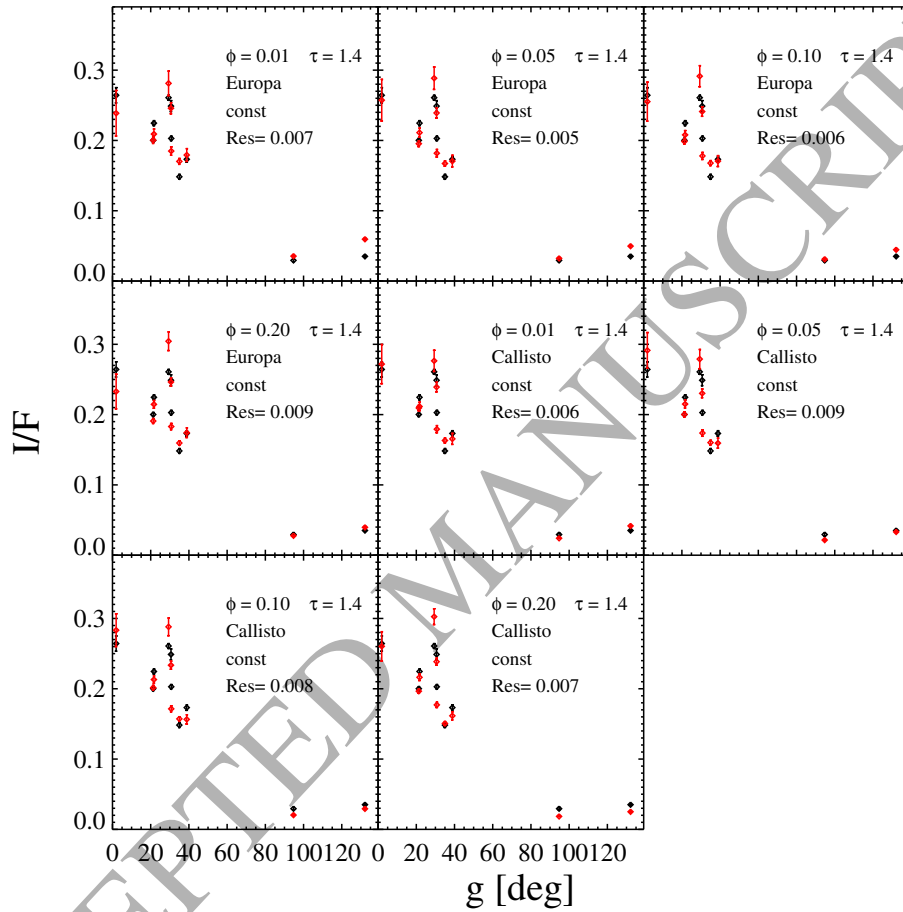
20
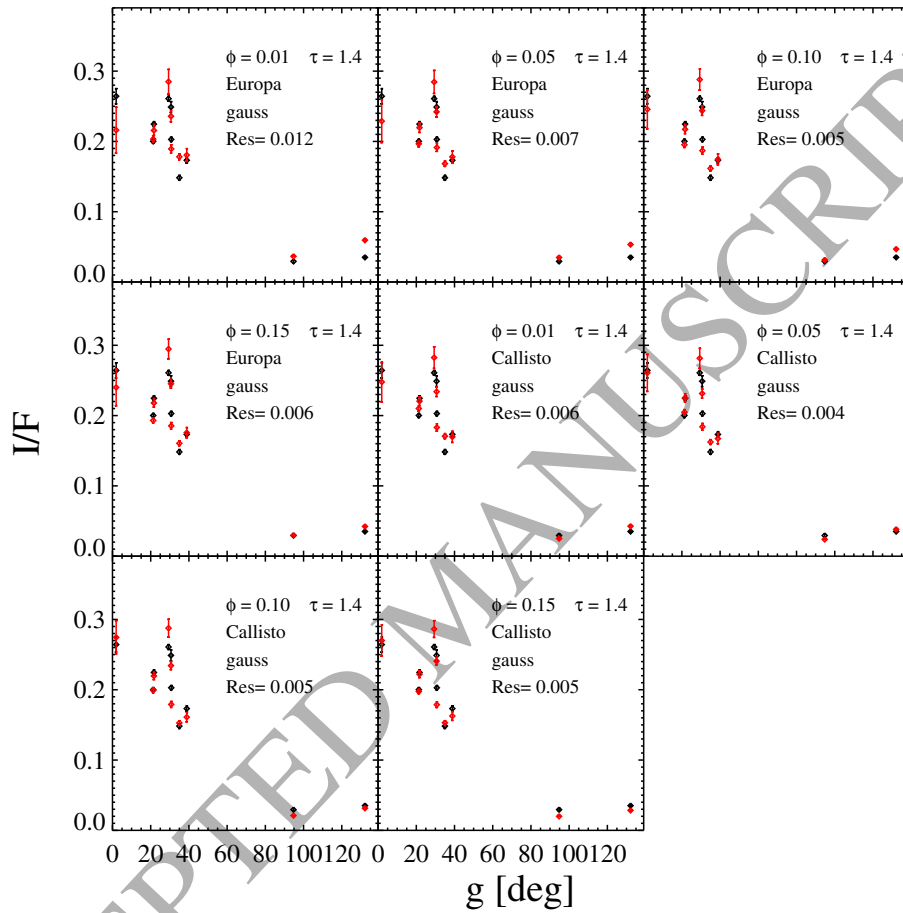
Figure 9: Fitted reflectance profiles at $\lambda = 0.55$ μm for B94300 region (red: Monte Carlo models; black: VIMS data), for various filling factors and SPPFs, as indicated in the plots. Filling factor profiles are assumed gaussian. The indicated value of ϕ refers to the average filling factor of the slab. The gaussian profile is defined such that the standard deviation is $\approx \frac{1}{6}$ of the total slab depth, thus providing $\phi \approx 0$ at slab boundaries. Error bars on Monte Carlo models are upper limits from uncertainties on observation geometry. The *Res* value is indicated and is calculated across the whole spectral range (see sec. 5).

21
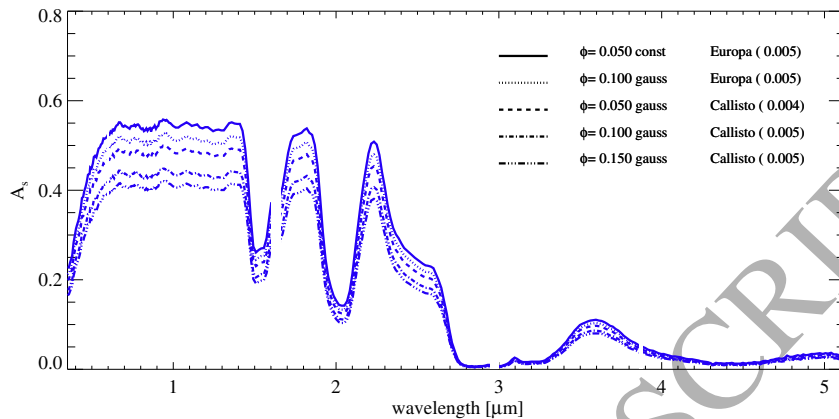
Figure 10: Best-fit spectral A_s's as derived from photometric fits of B94300 reflectance curves. The filling factor (average value and vertical profile type), phase function and *Res* value (in parenthesis) of the corresponding photometric models are indicated. Missing parts of the spectrum correspond to the instrument order sorting filters junctions.

overestimated with respect to the models with smaller average porosity ($\phi = 0.2 - 0.25$). The overall level of A_s is larger for the low filling factor solutions, indicating a compensation effect between porosity and Bond albedo (Fig. 13). Also in this case, in order to account for this variability, two final solutions are provided by separately averaging the high ($\phi = 0.2, 0.25$, B106700a) and low ($\phi = 0.05, 0.1$, B106700b) filling factor models (Fig. 17).

5.4. A131900

In Fig. 14 and 15 we report the best fits at 0.55 μm for a series of investigated models for the selected region in the A ring. Given the backscattering behavior of the phase curve we explore Callisto-like and Europa-like SPPFs and as for the B ring, we include models with both constant (Fig. 14) and gaussian (Fig. 15) filling factor profiles. In the second case, we explore up to an average $\phi = 0.05$, which, for $\tau = 0.6$, corresponds to a ring thickness of ≈ 8 particle diameters.

It can be noted that, for the A ring, the average quality of the photometric fit is worse with respect to the previous cases. A possible explanation of this can be represented by the observed azimuthal asymmetry in reflected light measured in the A ring (Dones et al., 1993; Salo et al., 2004; French

22

Figure 11: Fitted reflectance profiles at $\lambda = 0.55$ μm for B106700 region (red: Monte Carlo models; black: VIMS data), for various filling factors and SPPFs, as indicated in the plots. Filling factor profiles are assumed constant. Error bars on Monte Carlo models are upper limits from uncertainties on observation geometry. The *Res* value is indicated and is calculated across the whole spectral range (see sec. 5).
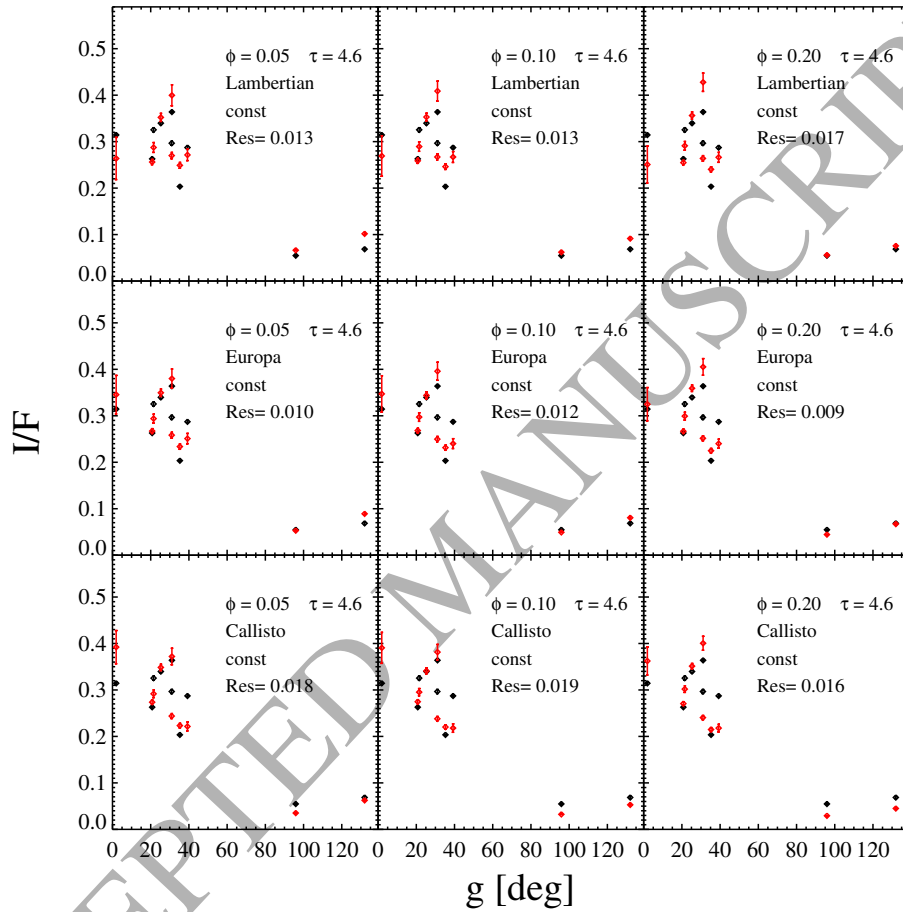
23

Figure 12: Fitted reflectance profiles at $\lambda = 0.55~\mu m$ for B106700 region (red: Monte Carlo models; black: VIMS data), for various filling factors and SPPFs, as indicated in the plots. Filling factor profiles are assumed gaussian. The indicated value of ϕ refers to the average filling factor of the slab. The gaussian profile is defined such that the standard deviation is $\approx \frac{1}{6}$ of the total slab depth, thus providing $\phi \approx 0$ at slab boundaries. Error bars on Monte Carlo models are upper and lower limits from uncertainties on observation geometry. The *Res* value is indicated and is calculated across the whole spectral range (see sec. 5).
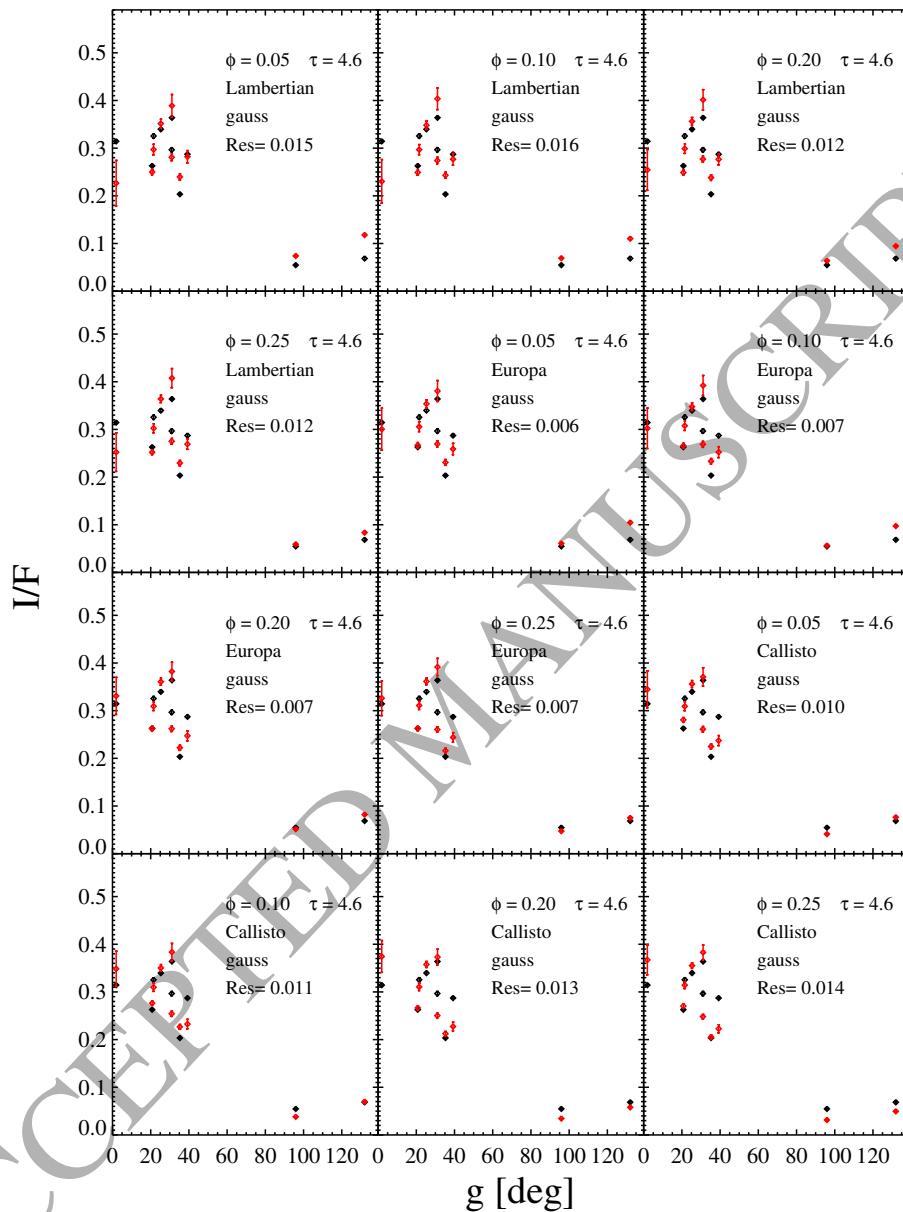
24
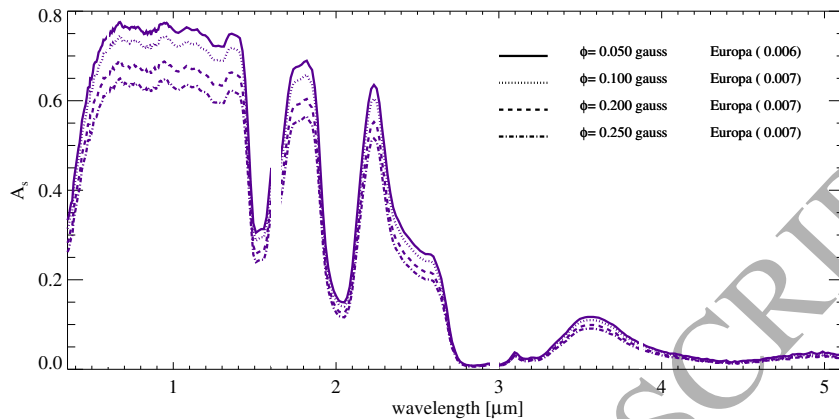
Figure 13: Best-fit spectral A_s's as derived from photometric fits of B106700 reflectance curves. The filling factor (average value and vertical profile type), phase function and Res value (in parenthesis) of the corresponding photometric models are indicated. Missing parts of the spectrum correspond to the instrument order sorting filters junctions.

et al., 2007a). Such an effect is induced by the presence of self-gravity wakes which produce a variation of the photometric output and depends on the observer elevation angle and on the wakes orientation with respect to the line of sight. The formation of gravity wakes can be modeled by means of N-body dynamical simulations (Salo et al., 2004), that are not included in the present analysis. The best matches ($Res \leq 0.018$) are obtained using the Callisto-like SPPF, with comparable results for the constants ($0.01 - 0.05 - 0.1$) and the gaussian (0.05) filling factors. As for the other investigated regions, the best-fit models show an anti-correlation between the estimated A_s and ϕ (Fig. 16). With the aim to account for this variability, also in this case, two different solutions are produced, representing a lower (A131900a) and an upper (A131900b) limit of the estimated albedo, by averaging separately the two models with the smallest ($\phi = 0.1$ $const$ and $\phi = 0.05$ $gauss$) and the largest ($\phi = 0.05$ $const$ and $\phi = 0.1$ $const$) spectral albedos, respectively (Fig. 17).

6. Phase dependent effects

As shown in Filacchione et al. (2014) spectral properties of the rings vary with observation geometry. In particular, it has been observed that spectral

25
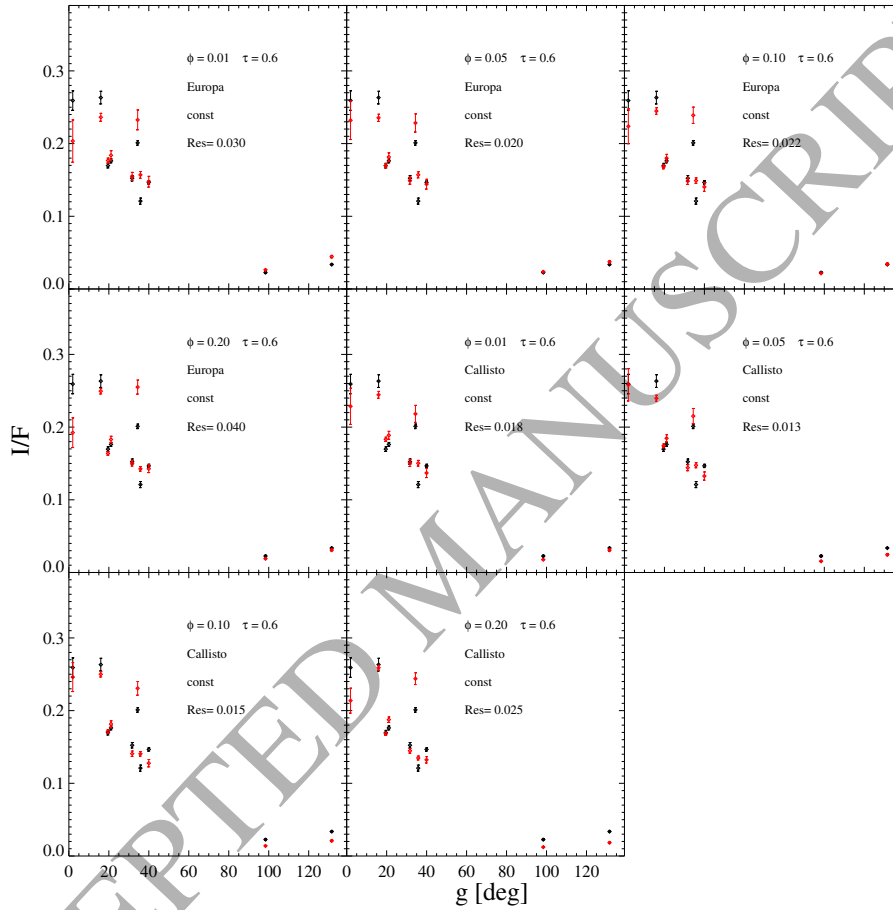
Figure 14: Fitted reflectance profiles at $\lambda = 0.55$ μm for A131900 region (red: Monte Carlo models; black: VIMS data), for various filling factors and SPPFs, as indicated in the plots. Filling factor profiles are assumed constant. Error bars on Monte Carlo models are upper limits from uncertainties on observation geometry. The *Res* value is indicated and is calculated across the whole spectral range (see sec. 5).
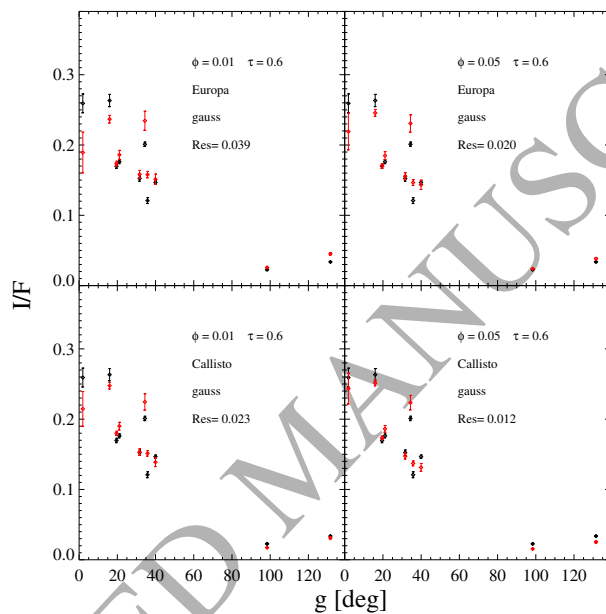
Figure 15: Fitted reflectance profiles at $\lambda = 0.55$ μm for A131900 region (red: Monte Carlo models; black: VIMS data), for various filling factors and SPPFs, as indicated in the plots. Filling factor profiles are assumed gaussian. The indicated value of ϕ refers to the average filling factor of the slab. The gaussian profile is defined such that the standard deviation is $\approx \frac{1}{6}$ of the total slab depth, thus providing $\phi \approx 0$ at slab boundaries. Error bars on Monte Carlo models are upper and lower limits from uncertainties on observation geometry. The *Res* value is indicated and is calculated across the whole spectral range (see sec. 5).

27
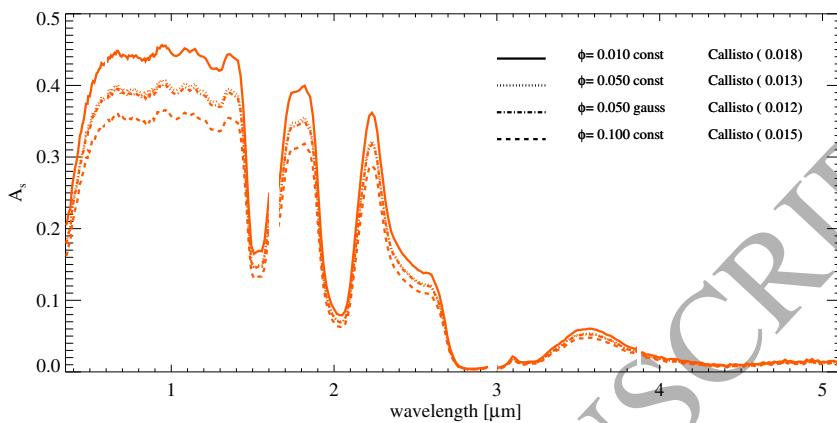
Figure 16: Best-fit spectral A_s's as derived from photometric fits of A131900 reflectance curves. The filling factor (average value and vertical profile type), phase function and Res value (in parenthesis) of the corresponding photometric models are indicated. Missing parts of the spectrum correspond to the instrument order sorting filters junctions.
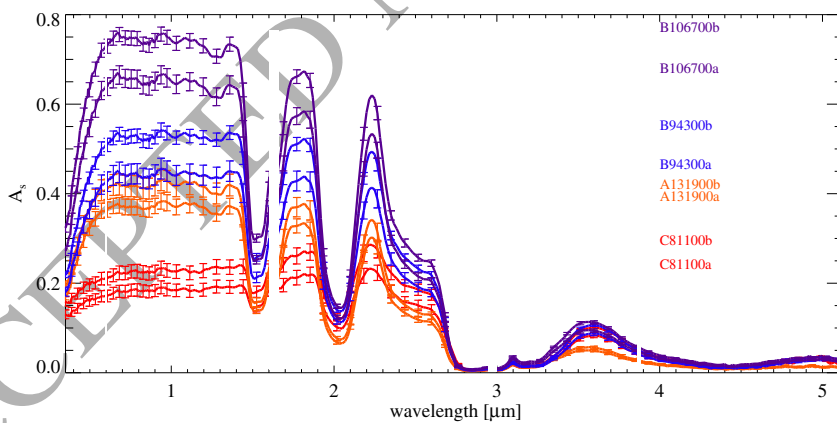
Figure 17: Final solutions for the spectral Bond albedo of the four investigated ring regions (indicated in the plot). Two solutions for each region have been derived, representing the two extremes of the model-dependent albedo variability (see Sec.5.1, 5.2, 5.3 and 5.4). Missing parts of the spectrum correspond to the instrument order sorting filters junctions.

28

slopes in the VIS-IR range and water absorption features at 1.5 μm and 2 μm increases with phase angle (Filacchione et al., 2012). Also Cuzzi et al. (2002) pointed out dependence of color ratios on phase angle, while they appear to be independent on the ring opening angle. A possible explanation for this behavior is represented by the different contribution of the multiply scattered component for different wavelengths, in accord with the albedo value, that introduces a spectral dependence on the reflectance phase curve. In this respect, two mechanisms can contribute to multiply scattered light: multiple scattering in the regolith covering ring particles and inter-particle scattering in the ring plane. For example, in the latter case, the expected effect can be described by the following reasoning. If we assume a back-scattering SPPF for the ring particles, the photometric output at small phase angles is dominated by light scattered once within the ring plane, while at high phase angles multiple scattering provides a larger contribution (see Fig. 1 and the variation of the reflectance curve shape at different albedos). If $A_S(\lambda_1) < A_S(\lambda_2)$ for the two different wavelengths λ_1, λ_2, the corresponding reflectance ratio $\frac{I/F_2(g,\lambda_2)}{I/F_1(g,\lambda_1)}$ increases with g because of the progressively larger contribution of multiple scattering at λ_2 with respect to λ_1. For a given shape of the Bond albedo spectrum such an effect will systematically provide a steepening of the spectral slope of the continuum and a deepening of the absorption features with the phase angle. Given this, we can then investigate whether inter-particle scattering explains the dependence of the ring spectral properties on phase angle. As an example we show in Fig. 18 the spectral slope in the VIS $S_{0.35-0.55}$, in the IR $S_{0.55-0.95}$ and the band depth BD at 1.5 μm, following the definition given in Filacchione et al. (2012) and Filacchione et al. (2014), as a function of the phase angle for selected models of the four investigated regions. It can be noted that the observed dependence on g is partially reproduced by simulations, indicating that inter-particle scattering contributes to this effect. This, on the other hand, does not exclude any additional contribution due to multiple scattering in the ring particles regolith, as suggested by Cuzzi et al. (2002).

It must be mentioned that an increase of the spectral slope with the phase angle, commonly referred to as "phase reddening" has been observed also in the case of very dark objects (Ciarniello et al., 2015; Ciarniello et al., 2017) and in laboratory measurements and reflectance simulations of low albedo/opaque samples (Schröder et al., 2014). This suggests another possible contribution, not necessarily related to the multiple scattering interaction, that produces

29

spectral variability with phase angle. Such a process could be responsible for the observed phase reddening of the C ring, which, although within the error, seems underestimated by our simulations, and partially for the A ring.

7. Spectral modeling

The retrieved spectral Bond albedos are reported in Fig. 17. For all the investigated regions water ice absorption features dominate the spectrum (1.5, 2 and 3 μm) while the continuum is characterized by a pronounced reddening towards short wavelengths, in the UV-VIS interval (0.35-0.55 μm). The continuum spectral slope at wavelengths longer than 0.55 μm changes sign passing from C81100 ring to B106700. In particular, the C ring appears to be redder with respect to the others rings, with a positive VIS-NIR spectral slope from 0.55 μm to 2.2 μm, water ice absorption features much less pronounced than B and A rings and the lowest average albedo. The C ring also presents the smallest reddening in the 0.35-0.55 μm interval. In the range 0.55-0.95 μm the spectral slope is neutral for B94300 and negative for B106700, while, beyond 1.5 μm, it is negative in both cases, with a larger absolute value for B106700, which has also the highest overall albedo. A131900 has a spectral behavior similar to B94300, with a lower albedo, but deeper 1.5 and 2 μm absorption features. The observed spectral reddening has been related to the presence of different contaminants in water ice, that separately affect the 0.35-0.55 μm and the 0.55-0.95 μm spectral slopes (Nicholson et al., 2008; Filacchione et al., 2014). In particular, as shown in the case of Saturn's moons, the UV-VIS absorption can be produced by different materials, including iron-bearing components (Clark et al., 2012) and carbon-rich organic compounds (tholins) (Cruikshank et al., 2005; Ciarniello et al., 2011). In addition to these, the overall albedo level and spectral features contrast can be determined by broad-band absorbers which also affect the VIS-NIR slope. Along with crystalline water ice (optical constants from Warren (1984); Mastrapa et al. (2009); Clark et al. (2012)) here we investigate a series of end-members (hereafter referred to as contaminants) of planetary interest which may prove significant for the ring spectral un-mixing. This is performed by applying the well-known Hapke's theory (Hapke, 1993), which allows to compute the SSA of a given mixture of different materials as a function of their optical constants, abundances, grain sizes and mixing modality (areal, intimate, intraparticle). The compounds selected for our analysis are

30
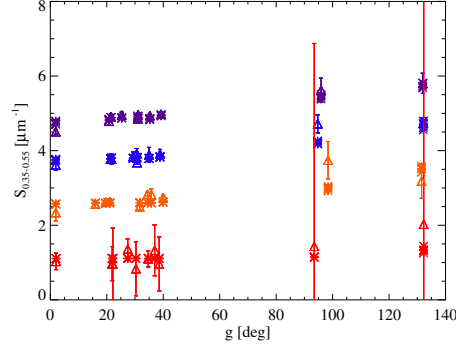
(a)
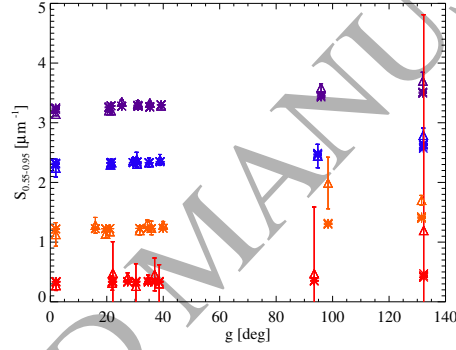
(b)
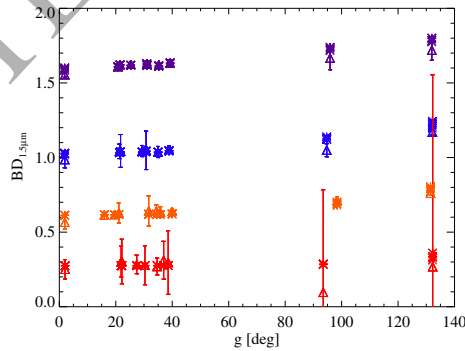
(c)

Figure 18: From top to bottom: Spectral slope in the VIS range $S_{0.35-0.55}$, in the IR $S_{0.55-0.95}$ and band depth at 1.5 μm $BD_{1.5\mu m}$ as a function of the phase angle for the four investigated regions: C81100 (red), B94300 (blue), B106700 (purple) and A131900 (orange). Asterisks represent all the selected simulations (see Secs. 5.1,5.2,5.3 and 5.4) and triangles are VIMS data. An offset of 2 μm^{-1} and 1 μm^{-1} has been added to the $S_{0.35-0.55}$ values of B106700 and B94300, respectively. An offset of 3 μm^{-1}, 2 μm^{-1} and 1 μm^{-1} has been added to the $S_{0.55-0.95}$ values of B106700, B94300 and A131900, respectively. $BD_{1.5\mu m}$ is offset for B106700 and B94300 of 1 and 0.5, respectively.

listed below, while their optical constants are shown in Fig. 19

- Tholin: these are macro-molecular solids formed by irradiation of organic compounds (CH_4,C_2H_6) often in presence of N_2. For our purpose we adopted a so called "Titan-tholin" (Khare et al., 1984; McDonald et al., 1994; Imanaka et al., 2004; Imanaka et al., 2012), obtained in gaseous phase from a 0.9:0.1 mixture of N_2/CH_4 (optical constants are from Cruikshank, personal communication)

- Hematite: nano-phase hydrated iron oxides with nano-phase metallic iron have been proposed by Clark et al. (2012) as an UV absorber for Iapetus, Phoebe, Hyperion, Dione, the F-ring and the Cassini Division. Here we adopt two sets of optical constants for iron oxides: one corresponding to nano-phase hydrated iron oxides from R. Clark (personal communication) and one from the average of crystalline hematite optical constants of the two sets presented by Sokolik and Toon (1999). It should be noted that crystalline hematite optical constants are significantly different from the nano-phase hydrated iron oxides with embedded nano-phase metallic iron proposed by Clark et al. (2012).

- Iron: sub-micron and nano-phase iron have been adopted in Clark et al. (2012) to model Iapetus spectrum. At larger grain size it is a viable candidate as a broad-band absorber. Here we assume optical constants reported in Clark et al. (2012).

- Troilite: iron sulfides have been proposed by Quirico et al. (2016) as opaque phases contributing to the extremely low albedo (0.06, Ciarniello et al. (2015)) of comet 67P. Troilite spectrum lacks diagnostic features from 0.3 to 2.6 μm (Britt et al., 1992) and is characterized by a red slope across this wavelength range. The optical constants used in this work are from Pollack et al. (1994) which reports the results derived from laboratory measurements in the 0.3 to 1 μm range by Egan and Hilgeman (1977) and extrapolated values at larger wavelengths.

- Silicates: in our analysis we consider both crystalline and amorphous silicates. For the former we assume optical constants by Pollack et al. (1994) while amorphous silicates (also referred to as "astronomical silicates") are described by the optical constants derived in Draine (2003).

32

- Amorphous carbon: similarly to iron, amorphous carbon is characterized by a low albedo and featureless spectrum across the investigated spectral range. Here we adopt the optical constants derived by Zubko et al. (1996), for hydrogenated amorphous carbon, obtained from arc discharge between carbon electrodes in H_2 atmosphere.
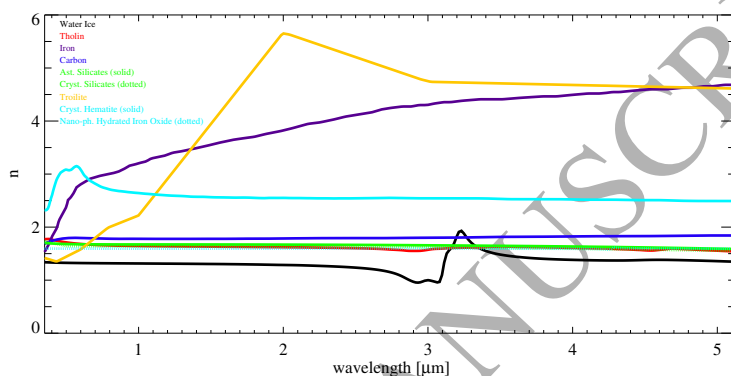
(a)
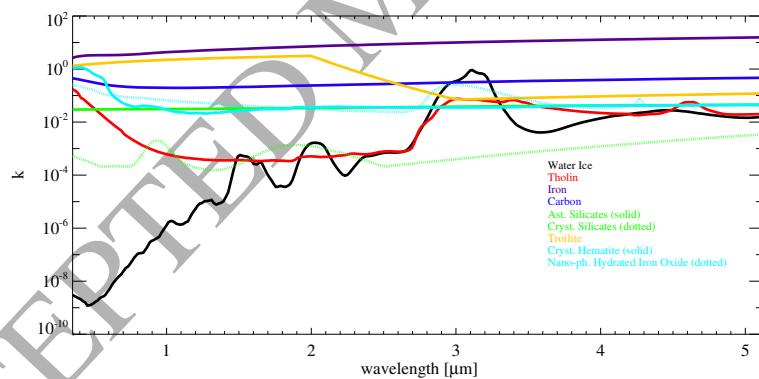
(b)

Figure 19: Real (top) and imaginary (bottom) part of the refractive index of different materials considered for ring spectral un-mixing.

As a first step for ring spectral inversion we assume a simple model made of an intimate mixture ("salt and pepper") of two different populations of particles. The first population is represented by icy grains embedding one of

33

the contaminants described above (intraparticle mixture, see Ciarniello et al. (2011) for further details on mixing modalities) while the second is either represented by one of the contaminants in pure form or by an ice-contaminant intraparticle mixture. As shown below, since all the contaminants investigated here are much more absorbing than water ice at short wavelengths, the first population is aimed to provide the UV absorption (UV absorber), while the second population of particle is meant to adjust the overall albedo level and spectral contrast (broad-band absorber), with an approach similar to Hedman et al. (2013).

In order to investigate the spectral effect of the various contaminants and mixing modalities on the modeled spectrum we show in Fig. 20 and Fig. 21 intimate mixtures of ice with different contaminants and ice-contaminant intraparticle mixtures, respectively, for variable end-members abundances. For the selected grain size (30 μm) it can be noted (Fig. 20) that adding pure amorphous carbon, or astronomical silicates to the mixture yields basically the same effect, with a reduction of the overall albedo and spectral contrast, and flattening of the spectral slope. A similar effect is given by crystalline hematite, which introduces a slightly blue slope across the spectrum and minor structures at shorter wavelengths. Conversely, crystalline silicates, even in small amounts ($\leq 5\%$) introduce the crystal field absorptions of Fe^{2+} at 0.9 μm. Along with a general reduction of the albedo, iron and troilite introduce a positive slope increasing with contaminant abundance. It can be also noted that iron increases the albedo at longer wavelengths. Finally, Titan tholin, produces a reduction of the albedo followed by a broad absorption feature shortward of 1 μm.

Ice-contaminant intraparticle mixtures are shown in Fig. 21. This mixing modality is more effective in modifying pure water ice spectral properties, with significant effects already at contaminant concentration well below 1%. In this case, although with a different magnitude, both amorphous carbon and amorphous silicate provide a broad absorption at smaller wavelengths with less than 0.1% abundance. Crystalline silicate, even in larger amounts, produce a much smaller spectral reddening, which is accompanied by the deepening of the 0.9 μm feature. Iron and troilite introduce a significant reddening of the spectrum, characterized by a positive slope extending from the VIS to the NIR. Crystalline hematite mixtures are characterized by a sharp downturn of the spectrum at wavelength below 0.7-0.8 μm, accompanied by a less steep slope extending beyond 1 μm. A different behavior is shown when the nano-phase form of the iron oxide is embedded in water ice,

34
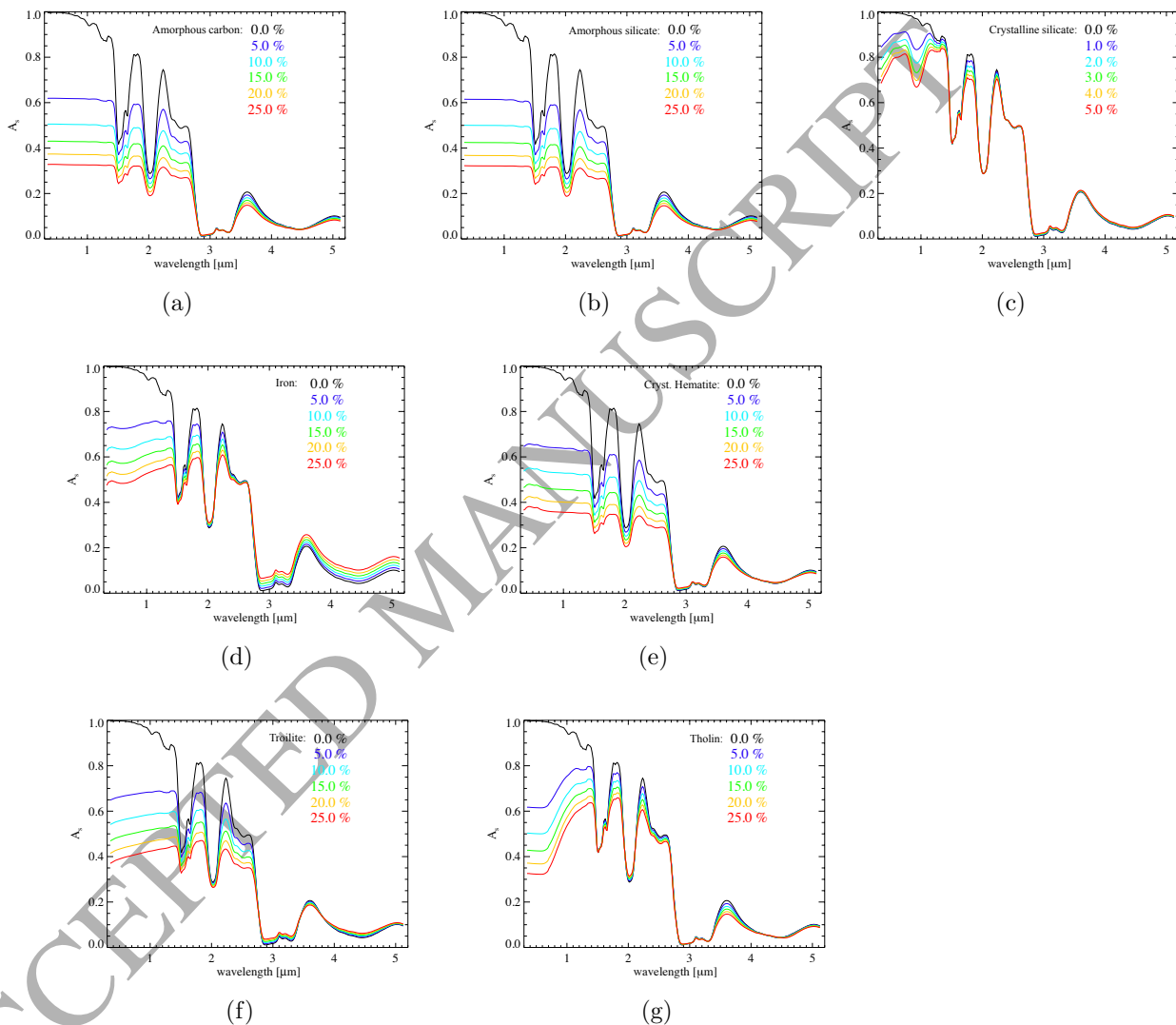
Figure 20: Intimate mixtures of ice and different contaminants. From left to right and top to bottom: carbon (a), amorphous silicate (b), crystalline silicate (c), iron (d), crystalline hematite (e), troilite (f) and titan tholin (g). The abundance of contaminant is indicated in the plots. Grain size is 30 μm.

35

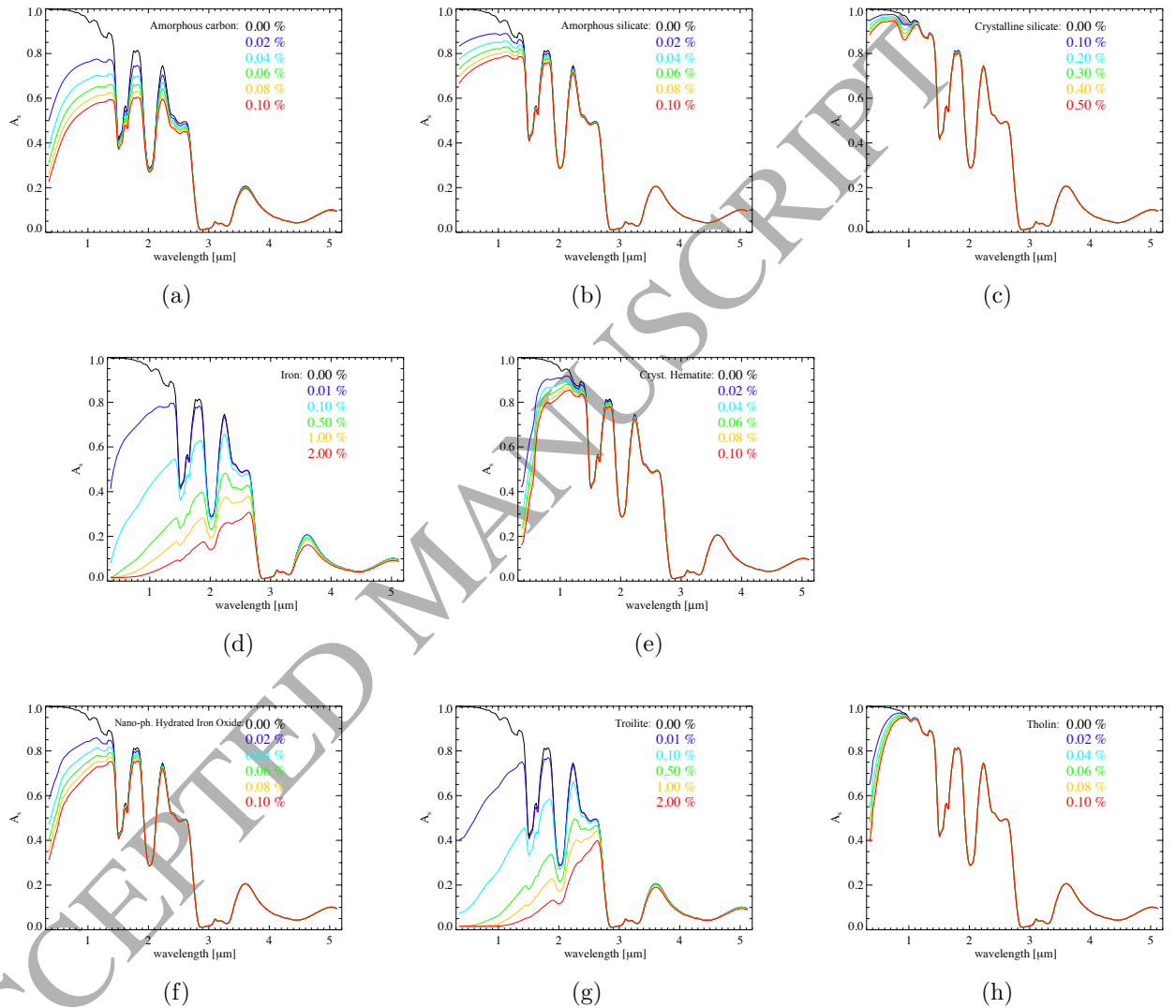Figure 21: Ice-contaminant intraparticle mixture. From left to right and top to bottom: carbon (a), amorphous silicate (b), crystalline silicate (c), iron (d), crystalline hematite (e), nano-phase hydrated iron oxide (f), troilite (g) and titan tholin (h). The abundance of contaminant is indicated in the plots. Grain size is 30 μm.

36

yelding an absorption qualitatively similar to iron, but less intense. Finally, tholin intraparticle mixtures show a relatively sharp reddening starting below 0.9-1 μm. According to these simulations, it can be noted that both crystalline hematite and tholin intraparticle mixtures show spectral properties that are compatible to the ones observed in the main rings at UV wavelengths.

7.1. Small icy particles

A quick comparison of the derived ring Bond albedo spectra (Fig. 17) with the simulations shown in Fig. 20 and 21 points out that large water ice grains exhibits a peak at 2.6 μm, which is not observed in the data. This issue was addressed in Clark et al. (2012) with the inclusion in the model of fine icy grains (micron-sized or small), which depress the 2.6 μm peak. Additional effects are a lower reflectance at longer wavelengths and a reduced 1.5 μm absorption feature. This difference is due to the possibility for small grains to partially develop light diffraction. In fact, in a particulate medium, large particles are in contact one each other and light diffraction is prevented (Hapke, 2012), while small grains can be relatively well separated. The SSA in the case of an isolated spherical particle can be be modeled by means of Mie theory, which naturally includes diffraction, thus leading to a different spectral output with respect to the case when diffraction is neglected, as shown in Clark et al. (2012), Fig. 22b of their paper.
Given this, we include in our spectral models a third population of ice sub-micron particles (grain size = 0.2 μm). For the computation of the SSA of the sub-micron component Mie theory is applied, while the particle geometric cross section is assumed as the extinction cross section of the grains.

7.2. B94300a initial spectral modeling

With the aim of selecting the most plausible ring compositional paradigm among the large number of possible scenarios available with the selected end-members, we performed a first spectral un-mixing of B94300a A_s spectrum, which exhibits intermediate spectral and albedo properties. The derived compositional paradigm will then be adopted to perform a more accurate spectral modeling and will be adapted to the other ring regions.

7.2.1. The UV absorber

In order to define the best candidate for the UV absorption, several models of B94300a were produced, with a mixture of different combinations of in-

37

traparticle ice-contaminant grains, pure amorphous carbon grains[2] and pure water ice sub-micron grains. As expected from the simulations shown in Fig. 21, reasonably good fits are obtained only when separately tholin or crystalline hematite are included[3]. In fig. 22 we show two best-fit models which include ice-tholin and ice-crystalline hematite particles, respectively. It can
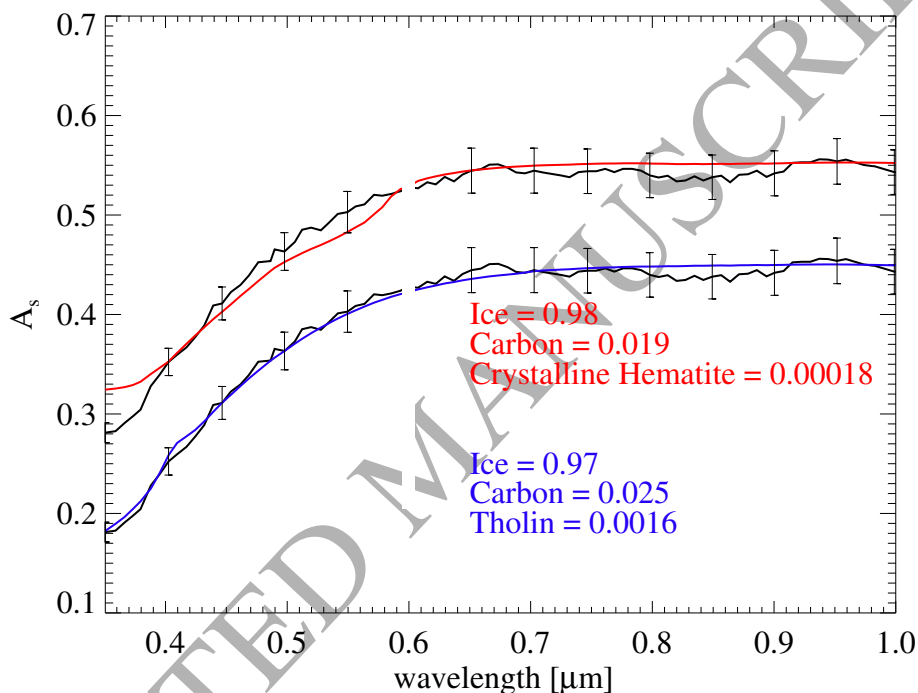
Figure 22: Best fit models with ice-tholin (blue) and ice-crystalline hematite (red) particles from 0.35 μm to 1 μm for B94300a. The volumetric abundances of the different end-members are indicated. In both cases, amorphous carbon is included to provide broadband absorption. For clarity, in the ice-crystalline hematite case both the B94300a and modeled spectra are shown with an offset of +0.1. The missing part of the spectrum corresponds to the instrument order sorting filters junction.

_____

[2]As shown later, the choice of amorphous carbon as a broad-band absorber does not affect the characterization of the UV absorption.

[3]For brevity, all the investigated models including the different contaminants embedded in water ice are not shown

be noted that the ice-crystalline hematite model does not fully match the measured spectrum at wavelengths <0.6 μm, being characterized by a less steep spectral slope. Based on this, we consider tholin as the best-fitting UV absorber, confirming the finding of Cuzzi et al. (2018). It must be mentioned that more complex models involving a larger number of free parameters (different grain sizes and populations) may provide good fits also with other compounds, such as nano-phase hydrated iron oxides and nano-phase iron, as shown by Clark et al. (2012) for Saturn's icy satellites, thus the identification of tholin as an UV absorber may not be definitive, although it gives the best match with the compositional paradigm adopted in this work. However, the non-unicity of the solutions from radiative transfer spectral inversion, is a well-known intrinsic limit of this approach, emphasized in the case of candidate end-members which are characterized by a limited number of diagnostic features in the investigated spectral range.

7.2.2. The broad-band absorber

Following the same approach of Sec. 7.2.1, models with ice-tholin grains and pure sub-micron ice mixed with a third population made of either pure contaminant or ice-contaminant grains have been analyzed, with the aim to select the best candidate as broad-band absorber.

- *Ice-tholin grains* and *sub-micron ice* mixed with *pure contaminants*: in Fig. 23 we report a series of best-fit models with Ice-tholin grains mixed with pure contaminants. In each plot we indicate the optical abundances of the different end-members, instead of volumetric fractions. This refers to the fractional cross section of a given end-member as seen by the propagating photon within the medium. The rationale of this choice is that the typical fitted grain size (from tens to hundreds of microns depending on the material) of the broad-band absorber is large enough to provide complete absorption of the light passing through the grains, making the spectral output not sensitive to the grain size. This means that for sizes larger than a given value, the corresponding volumetric abundances of the absorber can be arbitrarily large, without affecting the spectral output. Conversely, this is mostly driven by the optical abundance of the absorber, that is in fact fairly uniform among the different mixtures that produce good matches.
  It can be noted that amorphous carbon and amorphous silicates provide the best fits. The main differences between the modeled and measured

39

spectra are found at longer wavelengths (>2.7 μm) where amorphous carbon and amorphous silicates models match the average signal level, but only approximate the observed spectral shape. Possible explanations to this mismatch will be discussed later in Sec. 7.3. Mixtures with crystalline hematite produce a comparable match, although providing a slightly larger value of albedo at longer wavelengths, while tholin introduces a positive spectral slope in the continuum across 1 μm. Further testing for the other investigated regions of the rings reveals that these effects are more pronounced when larger amount of contaminants are required (C ring), providing a worsening in the spectral fit. Finally, mixtures with pure iron and troilite grains are not compatible with the ring spectrum. Crystalline silicates mixtures distinctly display the 0.9 μm and 1.9 μm absorption features and are not considered for brevity[4].

---

[4]According to our models these absorption features may fully saturate only assuming mm-sized grains

Figure 23: Best fit models with ice-tholin, sub-micron ice grains (sub) and pure contaminants. The optical abundances (see text) of Ice-thol+sub-micron ice grains and pure contaminant grains are indicated in parenthesis, while additional model details are in Tab. 1. For clarity, each model is shown with an offset of 0.25 from the one directly below. Missing parts of the spectrum correspond to the instrument order sorting filters junctions.

41

ACCEPTED MANUSCRIPT

Table 1: Spectral modeling parameters for mixtures reported in Fig. 23. Each row is identified by the pure contaminant intimately mixed with Ice-tholin grains and sub-micron ice grains. The volumetric fractions of the ice-tholin (Ice-thol), contaminant (Cont) and sub-micron ice (Sub-Ice) populations are indicated. The corresponding grain sizes of Ice-thol and Cont are in parenthesis. Finally, the fraction of tholin (f_{Thol}) embedded in ice-tholin and the optical abundances (opt. ab.) of Ice-thol+Sub-Ice and Cont are reported.

Contaminant	Ice-thol ($d[\mu m]$)	Cont ($d[\mu m]$)	Sub-Ice	f_{Thol}	Ice-thol+Sub-Ice opt. ab.	Cont opt. ab.
Crystalline Hematite	0.917 (111)	0.083 (25)	0.00089	0.0024	0.79	0.21
Tholin	0.717 (182)	0.283 (238)	0.00018	0.00074	0.8	0.2
Silicate	0.420 (109)	0.579 (500)	0.00032	0.0017	0.82	0.18
Carbon	0.852 (111)	0.148 (61)	0.00067	0.0018	0.82	0.18
Iron	0.919 (294)	0.081 (45)	0.00028	0.0017	0.71	0.29
Troilite	0.951 (195)	0.049 (18)	0.00048	0.0010	0.72	0.28

- *Ice-tholin grains* and *sub-micron ice* mixed with *ice-contaminant grains*:
  The required VIS-NIR absorption may be obtained, in principle, adding
  ice-contaminant grains to the ice-tholin and the sub-micron grains pop-
  ulations. Such a model requires one more free parameter, which is rep-
  resented by the fraction f_{Cont} of contaminant embedded in water ice. In
  Fig. 24 a series of best-fit models with ice-tholin grains and sub-micron
  ice grains mixed with ice-contaminants grains are shown. As for Fig.
  23, in each plot we indicate the optical abundances of the different end-
  members, along with the fraction f_{Cont} of the embedded contaminant.
  It can be noted that the fit quality is comparable to results obtained
  with intimate mixtures involving ice-tholin and pure contaminants. On
  the other hand, with the proper fraction of embedded contaminant, all
  the shown materials may provide reasonable fits. This is caused by the
  fact that the fraction f_{Cont} of the absorbing material and the grain size
  of the ice-contaminant population can be both adjusted to minimize
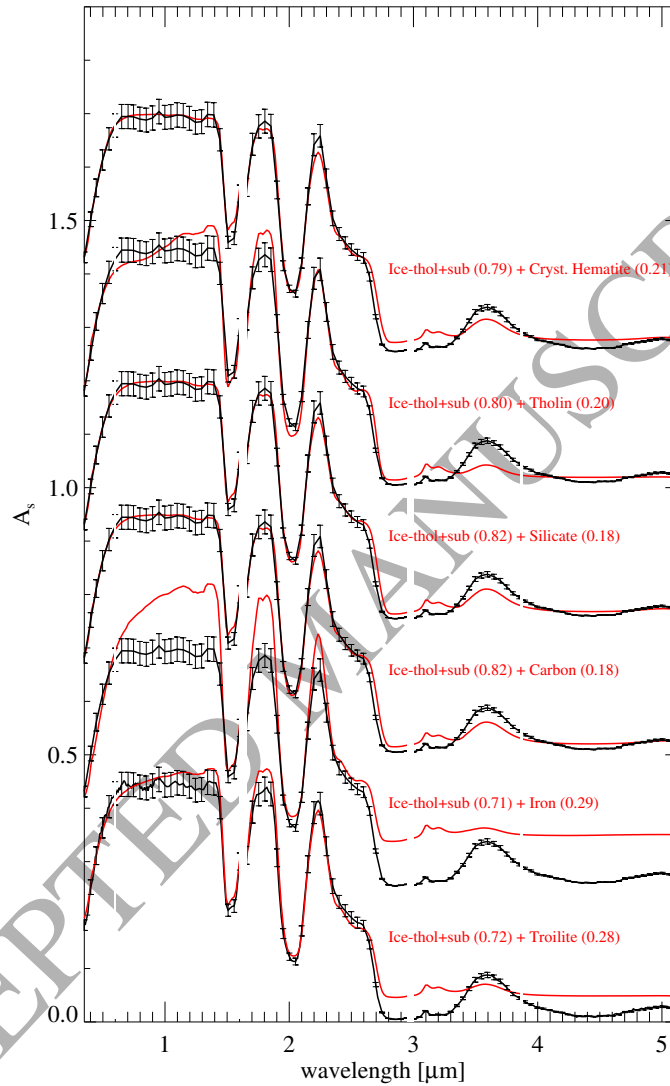 the corresponding spectral contrast.

43
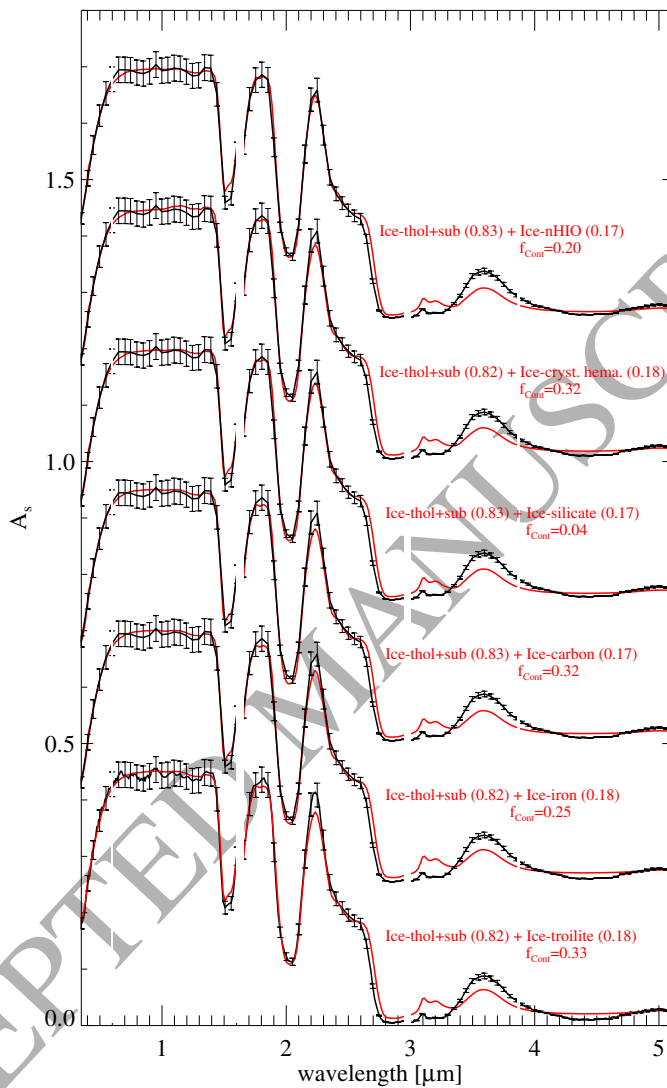
Figure 24: Best fit models with ice-tholin grains, sub-micron ice grains (sub) and ice-contaminant grains. The optical abundances (see text) of ice-thol+sub-micron grains and ice-contaminant grains are indicated in parenthesis, along with the fraction of contaminant embedded in ice (f_{Cont}). Additional model details are in Tab. 2. For clarity, each model is shown with an offset of 0.25 from the one directly below. Crystalline silicates mixtures are affected by the presence of 0.9 μm and 1.9 μm absorption features and are not shown for brevity, while nHIO indicates nano-phase Hydrated Iron Oxide. Missing parts of the spectrum correspond to the instrument order sorting filters junctions.

44

Table 2: Spectral modeling parameters for mixtures reported in Fig. 24. Each row is identified by the contaminant embedded in water ice grains which are intimately mixed with Ice-tholin grains and sub-micron ice grains. The volumetric fraction of the ice-tholin (Ice-thol), ice-contaminant (Ice-cont) and sub-micron ice (Sub-Ice) populations are indicated. The corresponding grain sizes of Ice-thol and Ice-cont are in parenthesis. Finally, the fraction of tholin (f_{Thol}) and contaminant (f_{Cont}) embedded in Ice-thol and Ice-Cont, respectively, and the optical abundances (opt. ab.) of Ice-thol+Sub-Ice and Ice-Cont are reported.

Contaminant	Ice-thol ($d[\mu m]$)	Ice-cont ($d[\mu m]$)	Sub-Ice	f_{Thol}	f_{Cont}	Ice-thol+Sub-ice opt. ab.	Ice-cont opt. ab.
nHIO	0.8225 (110)	0.1767 (74)	0.00084	0.0019	0.198	0.83	0.17
Crystalline Hematite	0.8416 (117)	0.1578 (71)	0.00061	0.0016	0.3236	0.82	0.18
Silicate	0.4510 (108)	0.5487 (450)	0.00035	0.0017	0.0394	0.83	0.17
Carbon	0.8954 (115)	0.1040 (48)	0.00058	0.0016	0.3248	0.83	0.17
Iron	0.8598 (115)	0.396 (60)	0.00061	0.0017	0.252	0.82	0.18
Troilite	0.8711 (116)	0.1283 (53)	0.00064	0.0016	0.333	0.82	0.18

45

From the comparison between the models reported in Fig. 23 and 24 it emerges that a unique determination of the population causing the VIS-NIR absorption in ring spectra cannot be achieved from this analysis. In particular, different end-members embedded in water ice or in pure form may provide the required nearly-neutral spectral properties. This is in fact indicated by the similar retrieved optical abundances of the VIS-NIR broad-band absorber (17-20%) among the different best-fitting models, which appears to not depend on the particular end-members and mixing modalities.

Given this, for the spectral modeling of the rings described in the following sections, we have assumed that the broad-band absorber is present in pure form, thus reducing the number of free parameters. Moreover, to be qualitatively consistent with the results of Cuzzi et al. (2018) we adopted amorphous carbon as the selected end-member. As described above, since the presented spectral modeling is not sensitive to the grain size of the broad-band absorber, we arbitrarily assume a grain diameter of 10 μm for the amorphous carbon particles. As show in Fig. 25 this size approximately represents a threshold beyond which all light passing through the single carbon grain is completely absorbed. From this argument it follows that the absolute volumetric amount of the broad-band absorber cannot be determined, being a model-dependent quantity. On the other hand, assuming that the contaminant properties (composition and grain size distribution) are the same across the rings, the resulting contaminant abundance is meaningful in relative terms.

7.3. B106700 spectral models

In Fig. 26a and 26b, we show the best fits obtained for the B106700 region for the two albedo solutions (B016700a and B106700b) derived from the photometric analysis, following the paradigm described in the previous section (7.2.2), with ice-tholin grains, pure water ice sub-micron particles and 10 μm size amorphous carbon grains. In each plot we show the best-fit (Sol1) and two extreme solutions (Sol2 and Sol3) in terms of water ice-tholin grain size, which provide a match with comparable accuracy, with the aim to constrain the range of variability of the free parameters in the model. The results are summarized in Tab. 3 and 4. According to the two sets of solutions the typical ice-tholin grain size is approximately in the range 60-130 μm while the volumetric amount of amorphous carbon varies in the 0.2-0.8% interval. The abundance of tholin embedded in water ice grains is 0.06-0.1%, while the optical abundance of amorphous carbon varies between 2-5%, de-
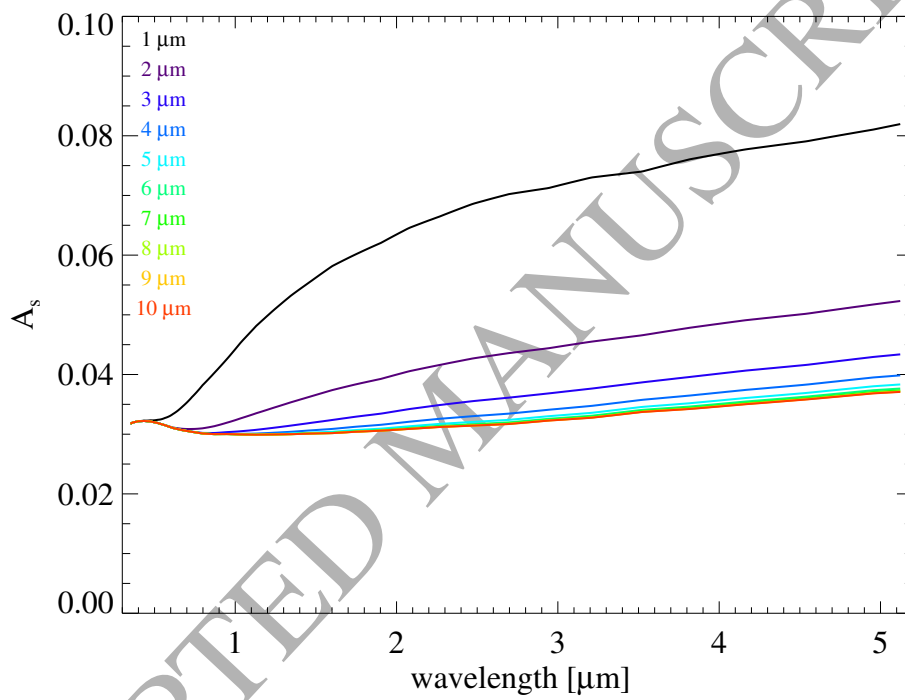
46

Figure 25: Modeled Bond albedo spectrum of amorphous carbon grains as a function of grain size (indicated in the plots). For grain sizes approaching $10\mu m$, A_s tends to a limit value.

47

pending on the overall albedo level. It can be noted that the match of the spectrum at longer wavelengths (>3 μm) is not fully satisfactory, although the albedo level is grossly matched. This is possibly related to a more complicated water ice size distribution than the one assumed here, with further populations of small grains (micron-sized and sub-micron sized). Moreover, the interpretation of the modeling result in this spectral region is further complicated by issues related with the assumed water ice optical constants. As stated above, for our analysis we take advantage of the optical constants from Clark et al. (2012), which in the IR part of the spectrum are derived from Mastrapa et al. (2009) after proper corrections. In particular, Clark et al. (2012) reports that original measurements in the 3-5.1 μm from Mastrapa et al. (2009) were affected by scattering contamination. The measured optical constants then have been modified in such a way that spectra simulated by means of Hapke theory, adopting the modified refractive indexes, where matched to laboratory reflectance spectra measurements on water ice grains. This effort produced improved optical constants, but their values may partially be affected by the particular set of parameters adopted in the Hapke models. Along with this, Filacchione et al. (2014) showed that ring spectral properties are affected by temperature variation on seasonal basis, with a significant effect on the position of the 3.6 μm peak. Temperature also produces a minor variation of the peak intensity (Clark et al., 2012). However, we cannot account for this variability in the present analysis, given that the observations investigated in this work have been acquired in different periods of Saturn's seasonal cycle. For these reasons, the result of the presented spectral modeling in 3-5.1 μm range, for the different investigated ring regions in this work, must be considered with caution. Finally, the models also do not fully match the larger strength of the 1.25 μm ice band, providing a further indication that more complex grain size distributions are needed to produce better fits. Although an impact of these issues on the interpretation of the contaminants abundances cannot be excluded, this should be of limited extent, since the derived amounts of the non-icy materials are mainly driven by the spectral behavior towards UV wavelengths and by the overall albedo level.

7.4. B94300 spectral models

In Fig. 27a and 27b, we show the best fits obtained for the B94300 region for the two albedo solutions (B94300a and B94300b) derived from the photometric analysis, following the paradigm described in Sec. 7.2.2. As for

48
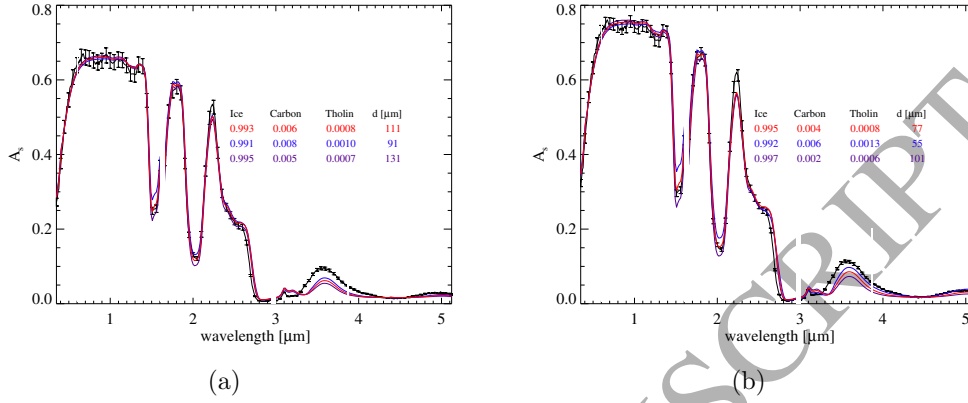
Figure 26: Spectral modeling of B106700a (left, black curve) and B106700b (right, black curve) Bond albedo. Red curves refer to Sol1 while blue and violet curves refer to Sol2 and Sol3, respectively. The total volumetric amounts of water ice, carbon and tholin are indicated, along with Ice-tholin grain size d. See tables 3 and 4 for further details.

Table 3: Spectral modeling retrieved parameters for B106700a. The volumetric abundances of Ice-tholin (Ice-thol), carbon and sub-micron ice (Sub-ice) are indicated, along with the carbon optical abundance (see Sec. 7.2.2). The total volumetric abundances of water ice and tholin are also reported, while f_{Thol} and d are the fraction of embedded tholin in ice-tholin grains and the ice-tholin grains diameter, respectively. Sol1 refers to the best fit model, while Sol2 and Sol3 are alternative solutions with comparable accuracy.

Solution	Ice-thol	Carbon	Sub-Ice	Ice	Tholin	f_{Thol}	d [μm]	carbon optical abundance
Sol1	0.9935	0.0059	0.00060	0.9933	0.00080	0.00080	111	0.047
Sol2	0.9910	0.0081	0.00098	0.9909	0.0010	0.0011	91	0.048
Sol3	0.9949	0.0046	0.00043	0.9947	0.00065	0.00066	131	0.045

Sec. 7.3, in each plot we show the best-fit (Sol1) and two extreme solutions (Sol2 and Sol3) in terms of water ice-tholin grain size which provide a match with comparable accuracy. The results are summarized in Tab. 5 and 6. According to the two sets of solutions the typical ice-thol grain size is approximately in the range 60-130 μm while volumetric amounts of amorphous carbon varies in the 1-3% interval. The abundance of tholin embedded in water ice grains is 0.1-0.2%. The optical abundance of amorphous carbon ranges between 10-18%, depending of the overall albedo level.

49

Table 4: Spectral modeling retrieved parameters for B106700b. The volumetric abundances of Ice-tholin (Ice-thol), carbon and sub-micron ice (Sub-ice) are indicated, along with the carbon optical abundance (see Sec. 7.2.2). The total volumetric abundances of water ice and tholin are also reported, while f_{Thol} and d are the fraction of embedded tholin in ice-tholin grains and the ice-tholin grains diameter, respectively. Sol1 refers to the best fit model, while Sol2 and Sol3 are alternative solutions with comparable accuracy.

| Solution	Ice-thol	Carbon	Sub-Ice	Ice	Tholin	f_{Thol}	$d\ [\mu m]$	carbon optical abundance
Sol1	0.9954	0.0037	0.00083	0.9954	0.00082	0.00082	77	0.021
Sol2	0.9917	0.0064	0.0019	0.9923	0.0013	0.0013	55	0.023
Sol3	0.9972	0.0024	0.00039	0.9970	0.00057	0.00058	101	0.020

Figure 27: Spectral modeling of 94300a (left, black curve) and B94300b (right, black curve) Bond albedo. Red curves refer to Sol1 while blue and violet curves refer to Sol2 and Sol3, respectively. The total volumetric amounts of water ice, carbon and tholin are indicated, along with ice-tholin grain size d. See tables 5 and 6 for further details. Missing parts of the spectrum correspond to the instrument order sorting filters junctions.

7.5. A131900 spectral models

In Fig. 28a and 28b, we show the best fits obtained for the A131900 region for the two albedo solutions (A131900a and A131900b) derived from the photometric analysis, following the paradigm described in the previous section (7.2.2). As for Sec. 7.3, in each plot we show the best-fit (Sol1) and two extreme solutions (Sol2 and Sol3) in terms of water ice-tholin grain size which provide a match with comparable accuracy. The results are summa-

50

Table 5: Spectral modeling retrieved parameters for B94300a. The volumetric abundances of Ice-tholin (Ice-thol), carbon and sub-micron ice (Sub-ice) are indicated, along with the carbon optical abundance (see Sec. 7.2.2). The total volumetric abundances of water ice and tholin are also reported, while f_{Thol} and d are the fraction of embedded tholin in ice-tholin grains and ice-tholin grains diameter, respectively. Sol1 refers to the best fit model, while Sol2 and Sol3 are alternative solutions with comparable accuracy.

Solution	Ice-thol	Carbon	Sub-Ice	Ice	Tholin	f_{Thol}	d [μm]	carbon optical abundance
Sol1	0.9731	0.0261	0.00070	0.9722	0.0016	0.0017	115	0.18
Sol2	0.9683	0.0308	0.0009	0.9673	0.0019	0.0020	102	0.18
Sol3	0.9764	0.0229	0.00058	0.9756	0.0015	0.0015	126	0.18

Table 6: Spectral modeling retrieved parameters for B94300b. The volumetric abundances of Ice-tholin (Ice-thol), carbon and sub-micron ice (Sub-ice) are indicated, along with the carbon optical abundance (see Sec. 7.2.2). The total volumetric abundances of water ice and tholin are also reported while f_{Thol} and d are the fraction of embedded tholin in ice-tholin grains and ice-tholin grains diameter, respectively. Sol1 refers to the best fit model, while Sol2 and Sol3 are alternative solutions with comparable accuracy.

Solution	Ice-thol	Carbon	Sub-Ice	Ice	Tholin	f_{Thol}	d [μm]	carbon optical abundance
Sol1	0.9797	0.0195	0.00086	0.9787	0.0017	0.0017	78	0.104
Sol2	0.9698	0.0286	0.0016	0.9691	0.0024	0.0025	60	0.105
Sol3	0.9853	0.0142	0.00048	0.9846	0.0012	0.0013	97	0.101

rized in Tab. 7 and 8. According to the two sets of solutions the typical ice-thol grain size is in the range 210-300 μm while volumetric amount of amorphous carbon varies in the 1.4-1.8% interval. The abundance of tholin embedded in water ice grains is 0.06%, with an approximately constant value for the different solutions. The optical abundance of amorphous carbon is in the 20-26% interval.

7.6. C81100 spectral models

C81100 spectral modeling performed by assuming the paradigm previously applied to B and A ring does not provide a good match of the observed spectral shape. In particular, the addition of a neutral spectrally-flat absorber is not able to reproduce the positive spectral slope that characterize C81100 spectrum up to 2.2 μm. In order to improve the spectral match an
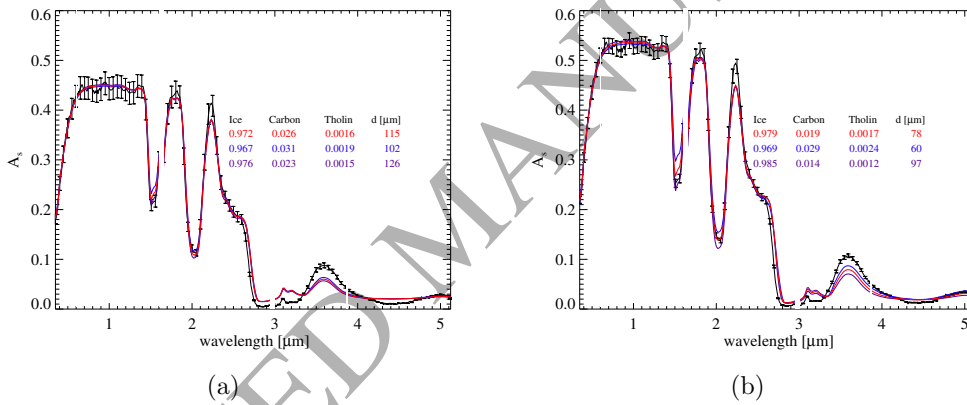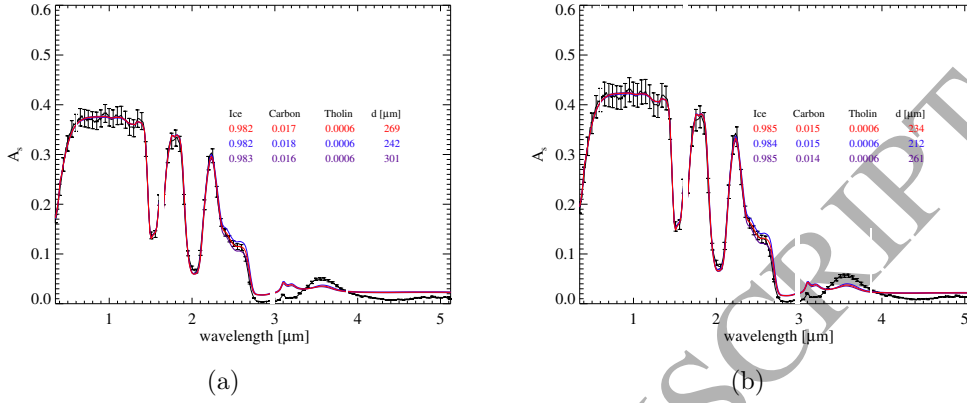
51

Figure 28: Spectral modeling of A131900a (left, black curve) and A131900b (right, black curve) Bond albedo. Red curves refer to Sol1 while blue and violet curves refer to Sol2 and Sol3, respectively. The total volumetric amounts of water ice, carbon and tholin are indicated, along with ice-tholin grain size d. See tables 7 and 8 for further details. Missing parts of the spectrum correspond to the instrument order sorting filters junctions.

Table 7: Spectral modeling retrieved parameters for A131900a. The volumetric abundances of Ice-tholin (Ice-thol), carbon and sub-micron ice (Sub-ice) are indicated, along with the carbon optical abundance (see Sec. 7.2.2). The total volumetric abundances of water ice and tholin are also reported, while f_{Thol} and d are the fraction of embedded tholin in ice-tholin grains and ice-tholin grains diameter, respectively. Sol1 refers to the best fit model, while Sol2 and Sol3 are alternative solutions with comparable accuracy.

Solution	Ice-thol	Carbon	Sub-Ice	Ice	Tholin	f_{Thol}	$d\ [\mu m]$	carbon optical abundance
Sol1	0.9838	0.0169	0.00026	0.9825	0.00061	0.00062	269	0.25
Sol2	0.9819	0.0178	0.00023	0.9815	0.00062	0.00063	242	0.26
Sol3	0.9835	0.0162	0.00031	0.9832	0.00062	0.00063	301	0.25

additional population of grains is required. Extensive analysis of the different possible scenarios indicate that the best match can be obtained by adding grains composed by water-ice embedding troilite inclusions (ice-troilite) or alternatively iron (ice-iron). In order to deal with a minimum number of free parameter this additional population is assumed to have the same grain size of ice-tholin grains. For brevity, below we show only the case including ice-troilite particles, but a brief discussion of ice-iron fits will be given as

52

Table 8: Spectral modeling retrieved parameters for A131900b. The volumetric abundances of Ice-tholin (Ice-thol), carbon and sub-micron ice (Sub-ice) are indicated, along with the carbon optical fraction (see Sec. 7.2.2). The total volumetric abundance of water ice and tholin are also reported while f_{Thol} and d are the fraction of embedded tholin in ice-tholin grains and ice-tholin grains diameter, respectively. Sol1 refers to the best fit model, while Sol2 and Sol3 are alternative solutions with comparable accuracy.

Solution	Ice-thol	Carbon	Sub-Ice	Ice	Tholin	f_{Thol}	d [μm]	carbon optical abundance
Sol1	0.9851	0.0145	0.00030	0.9848	0.00062	0.00063	234	0.20
Sol2	0.9843	0.0153	0.00027	0.9839	0.00063	0.00064	212	0.20
Sol3	0.9857	0.0139	0.00034	0.9854	0.00062	0.00063	261	0.20

well. The derived spectral models are in Fig. 29a and 29b, where we show the best-fit (Sol1) and two extreme solutions (Sol2 and Sol3), in terms of water ice-tholin grain size which provide a match with comparable accuracy. The results are summarized in Tab. 9 and 10. According to the two sets of solutions the typical ice-thol grain size results in the range 35-80 μm while the volumetric amount of amorphous carbon varies in the 7-13% interval. The abundance of tholin embedded in water ice grains is 0.2-0.6%, while the total amount of troilite is 0.6-1.5%. Ice-troilite grains in the mixture act as a broad-band absorber, as show in Fig. 21g, concurring with amorphous carbon to reduce the albedo level and introducing a positive spectral slope across the VIS-NIR spectral range. The optical abundance of amorphous carbon and ice-troilite grains varies between 14-30% and 25-29%, respectively, while their sum, which represent the total contributions of the darkening populations is 43-55%.

If ice-iron grains ($f_{Iron} = 0.023 - 0.027$) are adopted within the mixture instead of the ice-troilite population, spectral fits of similar quality are obtained. However, given the lower albedo of ice-iron grains, the abundance of amorphous carbon is typically shifted towards smaller amounts, with best-fits giving $\approx 3\%$ and $\approx 2\%$ for C81100a and C81100b, respectively. Similarly to the ice-troilite case, the total optical abundance of amorphous carbon grains and ice-iron grains is 44-54%.

53
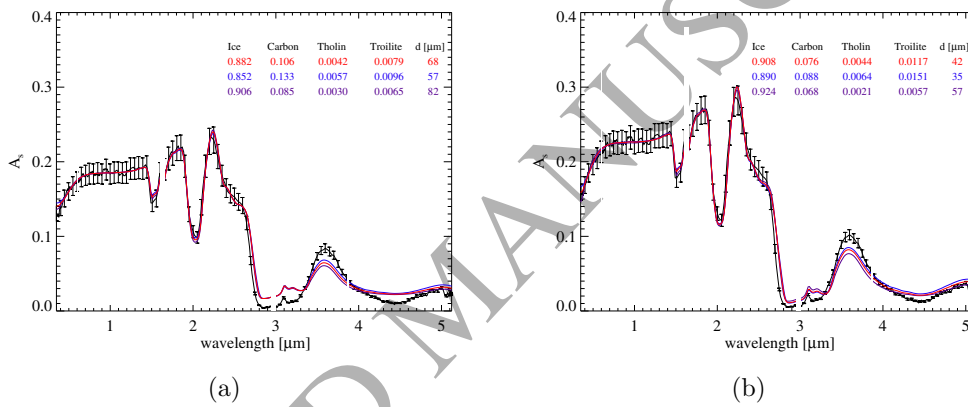
Figure 29: Spectral modeling of 81100a (left, black curve) and 81100b (right, black curve) Bond albedo. Red curves refer to Sol1 while blue and violet curves refer to Sol2 and Sol3, respectively. The total volumetric amounts of water ice, carbon, tholin and troilite are indicated, along with ice-tholin and ice-troilite grain size d. See tables 9 and 10 for further details. Missing parts of the spectrum correspond to the instrument order sorting filters junctions.

54

Table 9: Spetral modeling retrieved parameters for C81100a. The volumetric abundances of Ice-tholin (Ice-thol), carbon, sub-micron ice (Sub-ice) and Ice-troilite grains (Ice-tro) are indicated, along with the optical abundance of carbon and Ice-troilite grains (see Sec. 7.2.2). The total volumetric abundances of water ice, tholin and troilite are also reported while f_{Thol}, f_{Tro} and d are the fraction of embedded tholin in Ice-tholin, embedded troilite in Ice-troilite and the grains diameter of these populations, respectively. Sol1 refers to the best fit model, while Sol2 and Sol3 are alternative solutions with comparable accuracy.

Solution	Ice-thol	Carbon	Sub-Ice	Ice-tro	Ice	Tholin	f_{Thol}	Troilite	f_{Tro}	$d\ [\mu m]$	carbon optical ab.	Ice-tro optical ab.
Sol1	0.2610	0.1060	0.0025	0.6306	0.8818	0.0042	0.016	0.0079	0.013	68	0.29	0.26
Sol2	0.2374	0.1330	0.0031	0.6265	0.8518	0.0057	0.024	0.0096	0.015	57	0.30	0.25
Sol3	0.2840	0.0845	0.0019	0.6295	0.9060	0.0030	0.010	0.0065	0.010	82	0.29	0.26

Table 10: Spectral modeling retrieved parameters for C81100b. The volumetric abundances of Ice-tholin (Ice-thol), carbon, sub-micron ice (Sub-ice) and Ice-troilite grains (Ice-tro) are indicated, along with the optical abundance of carbon and Ice-troilite grains (see Sec. 7.2.2). The total volumetric abundances of water ice, tholin and troilite are also reported while f_{Thol}, f_{Tro} and d are the fraction of embedded tholin in Ice-tholin, embedded troilite in Ice-troilite and the grains diameter of these populations, respectively. Sol1 refers to the best fit model, while Sol2 and Sol3 are alternative solutions with comparable accuracy.

Solution	Ice-thol	Carbon	Sub-Ice	Ice-tro	Ice	Tholin	f_{Thol}	Troilite	f_{Tro}	d [μm]	carbon optical ab.	Ice-tro optical ab.
Sol1	0.3216	0.0758	0.0041	0.5985	0.9081	0.0044	0.014	0.012	0.020	42	0.15	0.28
Sol2	0.2755	0.0883	0.0054	0.6307	0.8901	0.0064	0.023	0.015	0.024	35	0.14	0.29
Sol3	0.4476	0.0676	0.0023	0.4825	0.9245	0.0021	0.0047	0.0057	0.012	57	0.20	0.25

7.7. Discussion

The results from spectral modeling of the retrieved Bond albedos for the four investigated regions are summarized in Fig. 30 and indicate that regolith composition varies across the ring plane but maintains elements of continuity. The paradigm of water ice mixed with tholin and amorphous carbon is able to reproduce the spectral behavior measured by VIMS in the densest rings. C ring modeling requires an additional population of particles, that may be represented either by ice with inclusions of troilite or ice embedding iron. The amount of tholin increases moving from A to the inner B ring with largest abundances in the C ring. In all the cases tholin is present in minimal amounts ranging from 0.06 to 0.6 %. The radial distribution of tholin in the ring plane is in good agreement with the one derived for the ring spectral UV absorber in Hedman et al. (2013), with the largest amounts measured in the inner B and C rings and suggests an intrinsic origin. In Hedman et al. (2013) the increase of the UV absorber in these regions has been related to a different plasma environment. In particular, Crary (2010) indicated that, for Saturn radial distances smaller than 99,000 km, particle orbits instabilities (Northrop and Hill, 1983; Jontof-Hutter and Hamilton, 2012) would deplete ring interior of negative ions. Such a modification in the ionization state of the ring population could have effects also in the chemical reactions and physical processes (e.g. radiolysis, photolysis) producing tholins.

More complicated is the interpretation of the abundance of the end-members that produce broad-band absorption within the rings. As mentioned above, the nature and the absolute amount of the broad-band absorber cannot be uniquely determined, depending dramatically on the mixing modalities of contaminants and their albedo properties, in particular when strongly absorbing materials are involved. While A and B rings can be modeled reasonably well by adding one population of absorbing grains (amorphous carbon in our models) to ice-tholin grains, C ring spectral modeling indicates that two populations of dark end-members (amorphous carbon and Ice-troilite or Ice-iron) are needed to match both the spectral slope at VIS-NIR wavelength and the albedo level. Moreover, it can be shown that for the A and B ring a similar spectral match can be achieved by replacing part of amorphous carbon with ice-troilite or ice-iron particles. Given this, we cannot draw quantitative conclusions on the analysis of the volumetric abundance of the broad-band absorber. Nonetheless, the progressive increase of the modeled amount of amorphous carbon with decreasing optical depth, should likely reflects, at least qualitatively, the distribution of the contaminants in the

57

rings. It must be mentioned that the modeling of A131900 ring is not fully aligned along this trend, showing carbon abundances compatible with the B94300 region. In this respect, it is important to notice that the derived ice-tholin grain size for A131900 is 2-3 times larger than the typical grain size of the other investigated regions, as required to match the deeper water ice absorption features. Such a large value of the grain size bias the volumetric abundance of amorphous carbon, whose diameter is assumed to be 10 μm, towards smaller amounts. Nonetheless, the spectral match at wavelength >3 μm for A131900 models, is the worst of the investigated dataset, indicating that, primarily for this case, a more realistic grain diameters distribution of the icy component, involving a larger fraction of smaller sizes, is needed.

A more robust parameter emerging from the spectral modeling described above is represented by the optical abundance of the darkening populations. It can be noted that this quantity is representative of the collective effect of the modeled parameters related to the darkening materials and strongly correlates with the overall albedo level, progressively decreasing with the optical depth τ of the investigated region. If we consider the optical abundance as a proxy of the total amount of contaminants, we confirm the finding reported in Hedman et al. (2013), indicating an increase of the broad-band absorber in ring spectra for low optical depths. The relation between optical depth and amount of contaminants can be linked to the mechanisms that darken the rings, like meteoroid bombardment (Cuzzi and Estrada, 1998), which are less effective in the denser regions, where a larger flux of impactors is required to produce a given level of contamination. In this perspective, the C ring spectral modeling involving troilite, may point towards contamination by cometary nuclei impacts. In the context of the discussion of the broad-band absorber distribution, it is also worth mentioning that results of Zhang et al. (2017a,b), from Cassini RADAR observations of the rings, indicate a trend of the non-icy material similar to the one derived in this work. In their analysis the contaminant is identified with silicates, and its amount is inversely related to the optical depth, with typical aboundances of $< 1\%$ for the A and B ring and $1 - 2\%$ in the C ring (maximum concentration of $6 - 11\%$). Such values are comparable with the total amount of the broad-band absorber derived in this work for the different regions of the rings.

In Cuzzi et al. (2017) the effect of surface roughness on the retrieved albedo of the observed objects has been discussed. In particular, surface reliefs and depressions on scales larger than the regolith grain size produce shadows that reduce the photometric output. If this effect is not considered the calculated

58

surface single scattering albedo can be underestimated. In Cuzzi et al. (2017) an analytic formulation of the shadowing law for spherical objects has been given and it has been shown that the integrated phase function of a body covered with a regolith following Lambert, Lommell-Seeliger or the Minnaert scattering law, in the presence of roughness, can converge to back-scattering functions, like the Callisto-like and Europa-like, which are the ones used in this work. In our modeling, with the aim to maintain a minimal number of free parameters, the conversion from Bond albedo to SSA has been derived by applying the Hapke's model and the similarity relations, without including the effect of roughness and determining, for a given A_S, the value of the regolith SPPF asymmetry parameter b that satisfied eq. 9. It must be noted that the derived values of the b parameter can partially account for not explicitly modeled roughness, mimicking the back-scattering dependence on phase angle induced by shadowing. However, this effect does not account for the reduction of integrated Bond albedo due to presence of shadows, thus the derived SSA values can be effectively underestimated. This leads to an overestimation of the optical abundance of contaminants in the spectral modeling, whose absolute value can be reduced with a corresponding increase of roughness. In the attempt to apply the roughness shadowing correction proposed by Cuzzi et al. (2017), we find that our derived Bond albedo must be divided by a factor $\xi = 0.43$ when Callisto-like phase function is assumed and by $\xi = 0.65$ for the Europa-like case[5]. Such values provide a roughness corrected albedo that for B106700a, B106700b and B94300a exceeds unity, preventing us to apply the correction. We argue that this is due to a combination of a possible overestimation of the derived albedo from Monte Carlo simulations and of the roughness effect in the formulation proposed by Cuzzi et al. (2017). In particular, one assumption in the derivation of the roughness shadowing correction is that in absence of surface roughness the ring particle phase function follows a Lambertian or Lommel-Seeliger law, which correspond to nearly isotropic or forward scattering regolith SPPF. If this hypothesis is relaxed allowing for back-scattering regolith SPPF, the extent of the shadowing roughness correction may be reduced. It is interesting to note that a good match of the B106700 phase function can be obtained only with an Europa-like particle phase function, while the other investigated re-

---

[5]Of the two formulations of the roughness shadowing corrections given in Cuzzi et al. (2017), here we apply the "Hapke-like" form, which produces a smaller effect

gions show behaviors which are compatible with a Callisto-like phase function (A131900) or have intermediate properties (C81100, B94300). This can be ascribed to the larger intrinsic albedo of B106700 particles, providing larger amount of multiple scattering among the facets composing their surfaces and reducing the effectiveness of roughness shadowing. This also indicates that at some level roughness shadowing effectively influences the photometric output of ring particles. Moreover, following this argument, we can hypothesize that the magnitude of the shadowing correction has a spectral dependence, being larger at wavelengths characterized by smaller albedos, where the minor contribution of inter-facets multiple scattering is less efficient in decreasing the roughness effects. Such a behavior would systematically reduce the spectral contrast, possibly leading to smaller grain sizes for the ice particles and/or reduced amounts of the UV absorber. Apart from the considerations reported above, we are not able to provide a quantitative determination of the roughness shadowing correction and of its effect on the absolute amount of contaminants in the different regions. However, given the limited variability of the derived particle phase function among the rings, it is likely that the distribution of the darkening material as obtained in our analysis is not affected in relative terms.

In Cuzzi et al. (2018), spectral modeling of the average UV spectra of the major rings is discussed. They propose a mixture of ice, ice-tholin, ice-carbon and ice-silicate to model the average A, B and C ring. Unfortunately, a quantitative comparison with Cuzzi et al. (2018) results, concerning the total amount of broad-band absorber, like carbon and silicates, cannot be performed, since as stated above, our modeling does not account for the shadowing correction. Moreover, our results are derived assuming an intimate mixing between icy grains and the broad-band absorbers while in Cuzzi et al. (2018) the mixing is intra-particle. In this respect, we have shown that the mixing modality, along with the contaminant grain size, plays a major role in assessing its corresponding volumetric amount. However, from a qualitative point view, we obtain a distribution of the contaminant in the ring plane in agreement with Cuzzi et al. (2018), with larger pollution in less dense regions, which is reassuring.

Conversely, a comparison on the derived amount of tholin between our results and Cuzzi et al. (2018) findings seems to be more significant, since the same mixing modality is adopted in the two works, and the amount of the UV absorber is less sensitive to the overall albedo in our modeling. We obtain tholin volumetric abundance ranging between $6 \times 10^{-4} - 6 \times 10^{-3}$, increas-

60

ing inward from A ring to C ring. These abundances overlap with results of Cuzzi et al. (2018), although in general our derived amounts are slightly smaller.

Spectrophotometric modeling of Saturn's rings at Far Ultraviolet (FUV) wavelengths is also discussed in Bradley et al. (2010) and Bradley et al. (2013), taking advantage of Cassini-UVIS observations (Esposito et al., 2004). In particular, Bradley et al. (2013), provided an estimation of the Bond albedo of the ring particles at 180 nm, for different regions in the ring plane. Maximum values of Bond albedo were obtained for the outer B ring, interpreted as a minimum amount of non-icy materials, while the C ring and Cassini Division, characterized by a smaller albedo, are likely richer in contaminants. This behavior is in qualitative agreement with our findings. A similar result is also reached in Bradley et al. (2010), where the UV spectral slope has been used as a proxy of the non-icy materials abundance. The typical scattering length derived in these works is of the order of $\approx 2 - 5\mu m$, corresponding to grain diameters up to 10 μm. Such values are much lower than the grain sizes derived in this work, and in general, from VIS-IR remote sensing observations of the rings (Filacchione et al., 2012; Filacchione et al., 2014). This difference, as suggested in Bradley et al. (2013), is possibly related to the fact that different wavelength regimes sample regolith at different depths (increasing from FUV to VIS-IR), and that the inferred scattering length, which is typically assumed as grain size, increases with wavelength (Cuzzi et al., 2018).

8. Summary and conclusions

In this work we investigated the spectrophotometric properties of Saturn's rings by means of Monte Carlo ray-tracing applied to VIMS observations. The dataset we used for our analysis consists of 10 radial mosaics of the rings that have been reduced and represented as spectrograms by Filacchione et al. (2014). Each spectrogram is characterized by a different observation geometry, thus for a selected radial distance from Saturn it was possible to build up a reflectance profile of a given region of the rings in the VIMS wavelength range. By comparing the reflectance profile to Monte Carlo ray-tracing simulations of light scattering in the ring plane we have been able to retrieve the spectral Bond albedo (A_s) and the single particle phase function ($P(g)$) of the ring particles, for four different regions: C81100, B94300, B106700 and
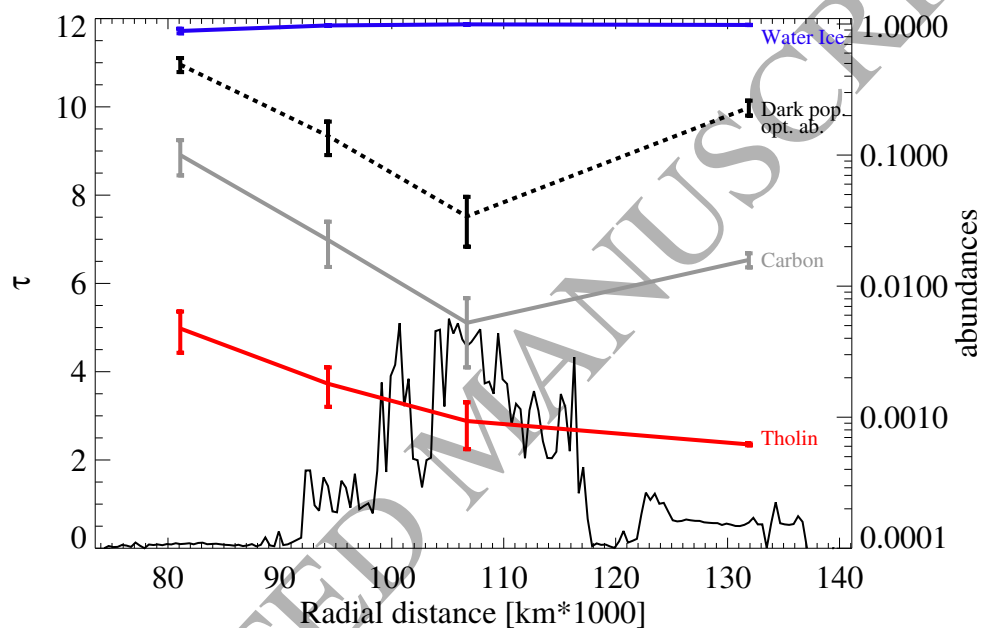
Figure 30: Abundances derived from spectral modeling as a function of the radial distance in the ring plane, compared to ring optical depth (black solid line). The total volumetric amount of water ice (blue), amorphous carbon (grey) and tholin (red) for the different investigated regions of the ring is shown, along with the optical abundance of the darkening populations (black dahsed curve; the darkening population is represented by amorphous carbon for A and B rings and amorphous carbon + Ice-troilite for the C ring). The bars on the curves represent the variability range for the different abundances.

62

A131900. The photometric analysis reveal that ring particles Bond albedo decreases with optical depth, with the highest values for the densest region in the B ring and minimum values in the C ring. The retrieved ring particles phase functions show a back-scattering behavior. The average photometric properties of the particles in the brightest of the two investigated B ring regions (B106700) are compatible with an Europa-like formulation of the phase function. For C81100 and B94300 both the Callisto-like and Europa-like may provide reasonable fits, while A131900 is best matched by a Callisto-like behavior. The spectral Bond albedo has been modeled by means of Hapke theory to infer rings' composition. We found that ring spectrum can be reproduced by water ice embedding with a UV absorber, which we model using tholins, with a variable amount of other absorbers in intimate or intraparticle mixture, and ice sub-micron grains. The UV absorber is present with minimal amounts (0.06-0.6 %), providing spectral reddening at short wavelengths. The identification of the other absorber(s) is uncertain, as well as its absolute abundance, however some conclusions on the relative distributions of this material in the ring plane can be drawn. A and B ring models suggest the presence of a neutral, low albedo component mixed with ice-tholin grains. C ring results suggests the presence of a third population, which is compatible with an intraparticle mixture of ice and iron-bearing materials (e.g. troilite, metallic iron), which is characterized by low albedo and a positive slope across the VIS-NIR range. The relative amount of these phases appears to be anti-correlated with optical-depth, pointing to an exogenous origin, likely driven by meteoroid or cometary bombardment as suggested by Cuzzi and Estrada (1998), which contaminates more effectively regions of low optical depth (C ring), where the pure ice reservoir and rejuvenation processes of ring particle surface are limited. Conversely, the distribution of the UV absorber is more compatible with an intrinsic origin, linked to the energetic processes (solar irradiation and interaction with charged particles) that drives their formation in the water ice particles. The relatively larger amounts of tholin measured in the inner B ring and C ring can be possibly related to the different plasma environment of these regions.

9. Acknowledgments

63

ACCEPTED MANUSCRIPT

64

10. References

References

Bradley, E.T., Colwell, J.E., Esposito, L.W., 2013. Scattering properties of Saturn's rings in the far ultraviolet from Cassini UVIS spectra. Icarus 225, 726–739.

Bradley, E.T., Colwell, J.E., Esposito, L.W., Cuzzi, J.N., Tollerud, H., Chambers, L., 2010. Far ultraviolet spectral properties of Saturn's rings from Cassini UVIS. Icarus 206, 458–466.

Britt, D.T., Bell, J.F., Haack, H., Scott, E.R.D., 1992. The Reflectance Spectrum of Troilite, in: Lunar and Planetary Science Conference.

Brown, R.H., Baines, K.H., Bellucci, G., Bibring, J.P., Buratti, B.J., Capaccioni, F., Cerroni, P., Clark, R.N., Coradini, A., Cruikshank, D.P., Drossart, P., Formisano, V., Jaumann, R., Langevin, Y., Matson, D.L., McCord, T.B., Mennella, V., Miller, E., Nelson, R.M., Nicholson, P.D., Sicardy, B., Sotin, C., 2004. The Cassini Visual and Infrared Mapping Spectrometer (VIMS) investigation. Space Sci. Rev. 115 (1-4), 111–168.

Chandrasekhar, S., 1960. Radiative transfer. Dover, New York.

Ciarniello, M., Capaccioni, F., Filacchione, G., 2014. A test of Hapke's model by means of Monte Carlo ray-tracing. Icarus 237, 293–305.

Ciarniello, M., Capaccioni, F., Filacchione, G., Clark, R., Cruikshank, D., Cerroni, P., Coradini, A., Brown, R., Buratti, B., Tosi, F., Stephan, K., 2011. Hapke modeling of Rhea surface properties through Cassini-VIMS spectra. Icarus 214, 541–555.

Ciarniello, M., Capaccioni, F., Filacchione, G., Raponi, A., Tosi, F., De Sanctis, M.C., Capria, M.T., Erard, S., Bockelee-Morvan, D., Leyrat, C., Arnold, G., Barucci, A. Beck, P., Bellucci, G., Fornasier, S., Longobardo, A., Mottola, S., Palomba, E., Quirico, E., Schmitt, B., 2015. Photometric properties of comet 67P/Churyumov-Gerasimenko from VIRTIS-M onboard Rosetta. Astronomy and Astrophysics 583.

Ciarniello, M., De Sanctis, M.C., Ammannito, E., Raponi, A., Longobardo, A., Palomba, E., Carrozzo, F.G., Tosi, F., Li, J.Y., Schröder, S.E., Zambon, F., Frigeri, A., Fonte, S., Giardino, M., Pieters, C.M., Raymond,

65

C.A., Russell, C.T., 2017. Spectrophotometric properties of dwarf planet Ceres from the VIR spectrometer on board the Dawn mission. A&A 598, A130. `1608.04643`.

Clark, R.N., Cruikshank, D.P., Jaumann, R., Brown, R.H., Stephan, K., Dalle Ore, C.M., Eric Livo, K., Pearson, N., Curchin, J.M., Hoefen, T.M., Buratti, B.J., Filacchione, G., Baines, K.H., Nicholson, P.D., 2012. The surface composition of Iapetus: Mapping results from Cassini VIMS. Icarus 218, 831–860.

Colwell, J.E., Esposito, L.W., Jerousek, R.G., Sremčević, M., Pettis, D., Bradley, E.T., 2010. Cassini UVIS Stellar Occultation Observations of Saturn's Rings. The Astronomical Journal 140, 1569–1578.

Crary, F., 2010. The B1/B2 Boundary and the Ring Ionosphere/Atmosphere, in: AAS/Division for Planetary Sciences Meeting Abstracts #42, p. 981.

Cruikshank, D.P., Owen, T.C., Ore, C.D., Geballe, T.R., Roush, T.L., de Bergh, C., Sandford, S.A., Poulet, F., Benedix, G.K., Emery, J.P., 2005. A spectroscopic study of the surfaces of Saturn's large satellites: H_2O ice, tholins, and minor constituents. Icarus 175, 268 – 283.

Cuzzi, J., Clark, R., Filacchione, G., French, R., Johnson, R., Marouf, E., Spilker, L., 2009. Saturn from Cassini-Huygens. Springer. chapter Ring Particle Composition and Size Distribution. p. 459.

Cuzzi, J.N., Chambers, L.B., Hendrix, A.R., 2017. Rough surfaces: Is the dark stuff just shadow?. ;Who knows what evil lurks in the hearts of men? The shadow knows!;. Icarus 289, 281–294.

Cuzzi, J.N., Estrada, P.R., 1998. Compositional Evolution of Saturn's Rings Due to Meteoroid Bombardment. Icarus 132, 1 – 35.

Cuzzi, J.N., French, R.G., Dones, L., 2002. HST Multicolor (255–1042 nm) Photometry of Saturn's Main Rings I: Radial Profiles, Phase and Opening Angle Variations, and Regional Spectra. Icarus 158, 199–223.

Cuzzi, J.N., French, R.G., Hendrix, A.R., Olson, D.M., Roush, T., Vahidinia, S., 2018. HST-STIS spectra and the redness of Saturn's rings. Icarus 309, 363–388.

66

Déau, E., 2015. The opposition effect in Saturn's main rings as seen by Cassini ISS: 2. Constraints on the ring particles and their regolith with analytical radiative transfer models. Icarus 253, 311–345.

Déau, E., Dones, L., Charnoz, S., West, R.A., Brahic, A., Decriem, J., Porco, C.C., 2013. The opposition effect in Saturn's main rings as seen by Cassini ISS: 1. Morphology of phase functions and dependence on the local optical depth. Icarus 226, 591–603.

Déau, E., Dones, L., Rodriguez, S., Charnoz, S., Brahic, A., 2009. The opposition effect in the outer solar system: A comparative study of the phase function morphology. Planetary and Space Science 57, 1282–1301.

Dones, L., Cuzzi, J.N., Showalter, M., 1993. Voyager Photometry of Saturn's A ring. Icaru 105, 184–215.

Draine, B.T., 2003. Scattering by Interstellar Dust Grains. I. Optical and Ultraviolet. ApJ 598, 1017–1025. astro-ph/0304060.

Egan, W.G., Hilgeman, T., 1977. The rings of Saturn - A frost-coated semi-conductor. Icarus 30, 413–421.

Esposito, L.W., Barth, C.A., Colwell, J.E., Lawrence, G.M., McClintock, W.E., Stewart, A.I.F., Keller, H.U., Korth, A., Lauche, H., Festou, M.C., Lane, A.L., Hansen, C.J., Maki, J.N., West, R.A., Jahn, H., Reulke, R., Warlich, K., Shemansky, D.E., Yung, Y.L., 2004. The Cassini Ultraviolet Imaging Spectrograph Investigation. Space Sci. Rev. 115, 299–361.

Filacchione, G., Capaccioni, F., Ciarniello, M., Clark, R.N., Cuzzi, J.N., Nicholson, P.D., Cruikshank, D.P., Hedman, M.M., Buratti, B.J., Lunine, J.I., Soderblom, L.A., Tosi, F., Cerroni, P., Brown, R.H., McCord, T.B., Jaumann, R., Stephan, K., Baines, K.H., Flamini, E., 2012. Saturn's icy satellites and rings investigated by cassini–vims: Iii –radial compositional variability. Icarus 220, 1064–1096.

Filacchione, G., Ciarniello, M., Capaccioni, F., Clark, R.N., Nicholson, P.D., Hedman, M.M., Cuzzi, J.N., Cruikshank, D.P., Dalle Ore, C.M., Brown, R.H., Cerroni, P., Altobelli, N., Spilker, L.J., 2014. Cassini-VIMS observations of Saturn's main rings: I. Spectral properties and temperature radial profiles variability with phase angle and elevation. Icarus 241, 45–65.

67

French, R.G., Salo, McGhee, C.A., Dones, L., 2007a. HST observations of azimuthal asymmetry in Saturn's rings. Icarus 189, 493–522.

French, R.G., Verbiscer, A., Salo, H., McGhee, C.A., Dones, L., 2007b. Saturn's Rings at True Opposition. Publications of the Astronomical Society of the Pacific 119, 623–642.

Hapke, B., 1993. Theory of reflectance and emittance spectroscopy. Topics in Remote Sensing, 3, Cambridge University Press, Cambridge, UK.

Hapke, B., 2008. Bidirectional reflectance spectroscopy: 6. Effects of porosity. Icarus 195, 918 – 926.

Hapke, B., 2012. Theory of reflectance and emittance spectroscopy. Cambridge University Press.

Hedman, M.M., Nicholson, P.D., Cuzzi, J.N., Clark, R.N., Filacchione, G., Capaccioni, F., Ciarniello, M., 2013. Connections between Spectra and Structure in Saturn's Main Rings Based on Cassini VIMS Data. Icarus 223, 105–130.

Henyey, L.G., Greenstein, J.L., 1941. Diffuse radiation in the Galaxy. Astrophys. J. 93, 70–83.

Van de Hulst, H., 1974. The spherical albedo of a planet covered with a homogeneus cloud layer. Astron. Astrophys. 35, 209–214.

Imanaka, H., Cruikshank, D.P., Khare, B.N., McKay, C.P., 2012. Optical constants of Titan tholins at mid-infrared wavelengths (2.5-25 μm) and the possible chemical nature of Titan's haze particles. Icarus 218, 247–261.

Imanaka, H., Khare, B.N., Elsila, J.E., Bakes, E.L., McKay, C.P., Cruikshank, D.P., Sugita, S., Matsui, T., Zare, R.N., 2004. Laboratory experiments of titan tholin formed in cold plasma at various pressures: implications for nitrogen-containing polycyclic aromatic compounds in titan haze. Icarus 168, 344–366.

Jontof-Hutter, D., Hamilton, D.P., 2012. The fate of sub-micron circumplanetary dust grains I: Aligned dipolar magnetic fields. Icarus 218, 420–432. 1201.3578.

68

Khare, B.N., Sagan, C., Arakawa, E.T., Suits, F., Callcott, T.A., Williams, M.W., 1984. Optical constants of organic tholins produced in a simulated Titanian atmosphere: From soft x-ray to microwave frequencies. Icarus 60, 127 – 137.

Lumme, K., Irvine, W.M., Esposito, L., 1983. Theoretical interpretation of the ground-based photometry of Saturn's B ring. Icarus 53, 174–184.

Mastrapa, R., Sandford, S.A., Roush, T.L., Cruikshank, D.P., Ore, C.M.D., 2009. Optical constants of amorphous, crystalline H_2O-ice: $2.5 - 22$ μm $(4000-455$ $cm^{-1})$ optical constants of H_2O-ice. Astrophys. J. 701, 1347–1356.

McCord, T., Coradini, A., Hibbitts, C., Capaccioni, F., Hansen, G., Filacchione, G., Clark, R., Cerroni, P., Brown, R., Baines, K., Bellucci, G., Bibring, J.P., Buratti, B., Bussoletti, E., Combes, M., Cruikshank, D., Drossart, P., Formisano, V., Jaumann, R., Langevin, Y., Matson, D., Nelson, R., Nicholson, P., Sicardy, B., Sotin, C., 2004. Cassini VIMS observations of the Galilean satellites including the VIMS calibration procedure. Icarus 172, 104 – 126. Cassini-Huygens at Jupiter.

McDonald, G.D., Thompson, W.R., Heinrich, M., Khare, B.N., Sagan, C., 1994. Chemical Investigation of Titan and Triton Tholins. Icarus 108, 137 – 145.

Miller, E., Klein, G., Juergens, D., Mehaffey, K., Oseas, J., Garcia, R., Giandomenico, A., Irigoyen, R., Hickok, R., Rosing, D., Sobel, H., Bruce, C., Flamini, E., DeVidi, R., Reininger, F., Dami, M., Soufflot, A., Langevin, Y., G.Huntzinger, 1996. The Visual and Ifrared Mapping Spectrometer for Cassini. SPIE 2803, 206.

Nicholson, P.D., Hedman, M.M., Clark, R.N., Showalter, M., Cruikshank, D.P., Cuzzi, J.N., Filacchione, G., Capaccioni, F., Cerroni, P., Hansen, G.B., Sicardy, B., Drossart, P., Brown, R.H., Buratti, B.J., Baines, K.H., Coradini, A., 2008. A close look at Saturn's rings with Cassini VIMS. Icarus 193, 182–212.

Northrop, T.G., Hill, J.R., 1983. The inner edge of Saturn's B ring. JGR 88, 6102–6108.

69

Pollack, J.B., Hollenbach, D., Beckwith, S., Simonelli, D.P., Roush, T., Fong, W., 1994. Composition and radiative properties of grains in molecular clouds and accretion disks. ApJ 421, 615–639.

Poulet, F., Cuzzi, J.N., 2002. The Composition of Saturn's Rings. Icarus 160, 350–358.

Poulet, F., Cuzzi, J.N., Cruikshank, D.P., Roush, T.L., Dalle Ore, C.M., 2002a. Comparison between the shkuratov and hapke scattering theories for solid planetary surfaces: Application to the surface composition of two centaurus. Icarus 160, 313–324.

Poulet, F., Cuzzi, J.N., French, R.G., Dones, L., 2002b. A Study of Saturn's Ring Phase Curves from HST Observations. Icarus 158, 224–248.

Quirico, E., Moroz, L.V., Schmitt, B., Arnold, G., Faure, M., Beck, P., Bonal, L., Ciarniello, M., Capaccioni, F., Filacchione, G., Erard, S., Leyrat, C., Bockelée-Morvan, D., Zinzi, A., Palomba, E., Drossart, P., Tosi, F., Capria, M.T., De Sanctis, M.C., Raponi, A., Fonti, S., Mancarella, F., Orofino, V., Barucci, A., Blecka, M.I., Carlson, R., Despan, D., Faure, A., Fornasier, S., Gudipati, M.S., Longobardo, A., Markus, K., Mennella, V., Merlin, F., Piccioni, G., Rousseau, B., Taylor, F., 2016. Refractory and semi-volatile organics at the surface of comet 67P/Churyumov-Gerasimenko: Insights from the VIRTIS/Rosetta imaging spectrometer. Icarus 272, 32–47.

Salo, H., 1995. Simulations of dense planetary rings. III. Self-gravitating identical particles. Icarus 117, 287–312.

Salo, H., French, R.G., 2010. The opposition and tilt effects of Saturn's rings from HST observations. Icarus 2010, 785–816.

Salo, H., Karjalainen, R., 2003. Photometric modeling of Saturn's rings I. Montecarlo method and the effect of nonzero volume filling factor. Icarus 163, 428–460.

Salo, H., Karjalainen, R., French, R.G., 2004. Photometric modeling of Saturn's rings. II. Azimuthal asymmetry in reflected and transmitted light. Icarus 179, 70–90.

70

Salo, H., Schmidt, J., Spahn, F., 2001. Viscous overstability in Saturn's B-ring: I. Direct simulations and measurement of transport coefficients. Icarus 153, 295–315.

Schröder, S.E., Grynko, Y., Pommerol, A., Keller, H.U., Thomas, N., Roush, T.L., 2014. Laboratory observations and simulations of phase reddening. Icarus 239, 201–216.

Shkuratov, Y.G., Stankevich, D.G., Petrov, D.V., Pinet, P.C., Cord, A.M., Daydou, Y.H., Chevrel, S.D., 2005. Interpreting photometry of regolith-like surfaces with different topographies: shadowing and multiple scattering. Icarus 173, 3–15.

Stankevich, D., Shkuratov, Y., 2004. Monte carlo ray-tracing simulation of light scattering in particulate media with optically contrast structure. Journal of Quantitative Spectroscopy and Radiative Transfer 87, 289 – 296.

Warren, S.G., 1984. Optical constants of ice from the ultraviolet to the microwave. Appl. Opt. 23, 1206–1225.

Zhang, Z., Hayes, A.G., Janssen, M.A., Nicholson, P.D., Cuzzi, J.N., de Pater, I., Dunn, D.E., 2017a. Exposure age of saturn's a and b rings, and the cassini division as suggested by their non-icy material content. Icarus 294, 14–42.

Zhang, Z., Hayes, A.G., Janssen, M.A., Nicholson, P.D., Cuzzi, J.N., de Pater, I., Dunn, D.E., Estrada, P.R., Hedman, M.M., 2017b. Cassini microwave observations provide clues to the origin of saturn's c ring. Icarus 281, 297–321.

Zubko, V.G., Mennella, V., Colangeli, L., Bussoletti, E., 1996. Optical constants of cosmic carbon analogue grains – I. Simulation of clustering by a modified continuous distribution of ellipsoids. Mon. Not. R. Astron. Soc 282, 1321–1329.